Faraday Discussions

Spiers Memorial Lecture: Next Generation Chalcogenide-Based Absorbers for Thin-Film Solar Cells

Journal:	*Faraday Discussions*
Manuscript ID	FD-ART-06-2022-000132.R1
Article Type:	Paper
Date Submitted by the Author:	01-Jul-2022
Complete List of Authors:	Mitzi, David; Duke University, Mechanical Engineering and Materials Science Kim, Yongshin; Duke University, Mechanical Engineering and Materials Science

Spiers Memorial Lecture: Next Generation Chalcogenide-Based Absorbers for Thin-Film Solar Cells

David B. Mitzi[1,2,] and Yongshin Kim[1]*

[1]Department of Mechanical Engineering and Materials Science, Duke University, Durham, North Carolina 27708, USA.

[2]Department of Chemistry, Duke University, Durham, North Carolina 27708, USA.

E-mail: david.mitzi@duke.edu

Abstract

Inorganic-based thin-film photovoltaics (TFPV) represents an important component of the growing low-carbon energy market and plays a vital role in the drive toward lower cost and increased penetration of solar energy. Yet, commercialized thin-film absorber technologies suffer from some non-ideal characteristics, such as toxic or non-abundant element use (e.g., CdTe and $Cu_2(Ga,In)(S,Se)_2$), which bring into question their suitability for terawatt deployment. Numerous promising chalcogenide, halide, pnictide and oxide semiconductors are being pursued to bridge these concerns for TFPV and several promising paths have emerged, both as prospective replacements for the entrenched technologies, as well as to serve as a partner (i.e., higher bandgap) absorber for a tandem junction device—e.g., to be used with a lower bandgap Si bottom cell. The current perspective will primarily focus on emerging chalcogenide-based technologies and provide both an overview of absorber candidates that have been of recent interest, as well as a deeper dive into an exemplary Cu_2BaSnS_4-related family. Overall, considering the combined needs of high-performance, low-cost, and operational stability, as well as the experiences gained from existing commercialized thin-film absorber technologies, chalcogenide-based semiconductors represent a promising direction for future PV development and also serve to highlight common themes and needs among the broader TFPV materials family.

1. Introduction

The target of pervasive solar photovoltaics (PV) provides one of the cornerstones in the global transition to a clean and carbon-neutral energy future.[1] In 2020, 3.2% of global electricity was derived from installed solar modules, representing substantial growth over the last 10 years, but still leaving vast need for further progress to overtake, for example, coal, which represented 35% of electricity generation in the same period.[2] Thin-film photovoltaics (TFPV) accounts for <6% of the overall PV market in 2020, with the remainder arising predominantly from competing silicon-based modules.[3] Despite the relatively small current market share, a fundamental basis of the current discussion on "Emerging Inorganic Materials in Thin-Film Photovoltaics" relates to the notion that TFPV offers a compelling pathway towards more cost-competitive and pervasive PV deployment relative to entrenched silicon PV and carbon-based electricity generation. This conviction follows in part from: 1) the substantially lower volumes of material needed to prepare an effective "absorber" within TFPV devices relative to silicon (i.e., the technology relies on ~1 μm rather than ~100 μm layer thickness, respectively), 2) monolithic integration enabling high throughput, lower cost manufacturing for TFPV (not an option for crystalline silicon), 3) high performance (>20 % efficiency in converting the AM 1.5G spectrum to electrical power) and a high degree of reliability having already been demonstrated for several commercialized TFPV technologies, and 4) the "thin" nature of TFPV providing natural opportunities for a larger range of form factors—e.g., flexible, partially transparent, and building integrated PV. Finally, making use of the broader bandgap range offered by TFPV and the potential for relatively low-temperature and low-cost processing also opens the opportunity to merge high efficiency crystalline silicon PV with higher bandgap TFPV devices in tandem PV configurations, in an effort to target power conversion efficiency (PCE) levels >30%.[4]

Over the last 20 years, three TFPV technologies have dominated commercial markets: amorphous silicon (a-Si), CdTe and $Cu(In,Ga)(S,Se)_2$ (CIGS). While a-Si was by far dominant in the early- to mid-2000s timeframe, inherent performance limitations associated with the amorphous nature of this semiconductor at least in part promoted the rise of the chalcogenide-based systems, which by the current time (after mid-2010s) overwhelmingly have dominated the marketplace.[3] The largest manufacturer of thin-film (i.e., CdTe) modules is First Solar, which produced 7.9 GW of PV modules in 2021 (the company estimates that their CdTe module uses approximately 2% of the semiconductor material as compared to a crystalline silicon module).[5] Despite the growth in CdTe (and to a lesser extent CIGS) in the marketplace, concerns remain regarding extended scalability of these technologies to TW levels, given the toxic nature of Cd (also associated regulations) and relative scarcity of Te and In in the earth's crust. Given this, there is considerable interest in identifying alternative semiconductors that may serve as replacements for CdTe and CIGS in the on-going expansion of TFPV deployment. As a basis of this search, any prospective TFPV alternative needs to offer, at a minimum, the following materials characteristics: 1) High absorption coefficient ($>10^4$ cm^{-1}) over the relevant spectral range covered by the AM 1.5G solar spectrum, which generally implies the need for a direct or quasi-direct bandgap in the range of E_g = 1.0-1.6 eV for single-junction devices; 2) reasonably small effective masses for electrons/holes in the semiconductor to facilitate photogenerated carrier collection, which entails

substantial valence/conduction band dispersion at the band edges; 3) Enhanced minority carrier lifetimes to provide for adequate minority carrier diffusion lengths (i.e., ideally these should be a significant fraction of the full absorber layer thickness), which implies that defects within the semiconductor will not introduce an appreciable concentration of deep levels; and 4) sufficient chemical/environmental stability to underlie a targeted module operational lifetime of 25-40 yrs (for utility or roof-mounted residential/commercial application, this generally implies a loss of <20% of the rated performance level over this period).[6]

Beyond these requirements, commercial success also requires that the developed materials systems be compatible with ultra-low-cost and high-throughput fabrication, with low energy input (lowers the energy payback time for the technology), and the search should ideally focus on technologies that do not rely on highly toxic or constrained supply (i.e., scarce in the Earth's crust, difficult to extract, or geographically/geopolitically limited in terms of supply source) elements. Importantly, the success of an absorber choice depends on the compatibility (i.e., chemical, band alignment, doping type and levels) with other device layers.[7] Further, if the emerging absorbers are compatible with overall device structures (i.e., other layers of the device beyond the absorber) that are already being commercially produced, this will facilitate acceptance within the marketplace, since this means that significant components of the production facility can remain nominally unchanged (i.e., less capital expenditure needed to adopt the new technology). The remainder of this discussion will give a brief glimpse into some of the systems being explored as emerging TFPV absorbers. Section 2 provides a selective summary of some absorber systems that have received recent attention, while Sections 3 and 4 provide a deeper dive into a specific family of multinary chalcogenide systems with which the authors have been particularly involved over the last few years. Finally, Section 5 concludes and provides some broader perspectives and open questions for the future in this area.

2. Emerging Thin-Film Photovoltaics Contenders

A rich array of exciting prospects for thin-film absorbers are currently being explored, which span a wide chemical space, bandgap range and degree of development. There have been numerous recent and informative reviews of these options.[8-12] In this section, we will briefly examine several selected systems that have been of most significant *recent interest*, with an emphasis on *chalcogenide-based* absorbers. Notably, several systems that played an important early role in chalcogenide-based TFPV material development, Cu_2S and pyrite (Fe_2S_3),[13-17] are not explored in the current review. Further, we will restrict the discussion to bulk (i.e., contrasting with nanocrystal-based approaches wherein quantum confinement plays an important role[18-20]) absorbers and those systems for which successful PV devices have already been demonstrated (i.e., neglecting the important field of theoretically predicted solar absorber materials, if the predicted systems have not been experimentally demonstrated[21-23]).

2.1 Sb_2S_3 / Sb_2Se_3. Given the success of CdTe technology, including available facile low-cost vacuum-based processing approaches and record cell efficiencies already exceeding 20%, there is great interest in identifying alternative binary chalcogenides that offer similar advantages without

the toxicity and elemental abundance issues associated with Cd and Te.[12] In this respect, antimony chalcogenides (Sb_2Se_3 and Sb_2S_3) represent one compelling research direction.[24-26] These semiconductors offer strong absorption (>10^4 cm^{-1}) and bandgaps that are highly suitable for either single junction (~1.1 eV for Sb_2Se_3) or multijunction (~1.7 eV for Sb_2S_3) PV devices. In contrast to the nominally isotropic (3D) crystal structure of CdTe, Sb_2X_3 (X=S, Se) structures comprise nominally 1D $(Sb_4X_6)_n$ ribbons extending along the (001) crystallographic direction (**Figure 1a**), with Sb in both trigonal and square pyramidal coordination, and weaker interactions among these ribbons. The anisotropic crystal structure gives rise to band structure anisotropy, with substantial band dispersion associated with the (001) crystallographic direction and less significant dispersion in orthogonal directions (**Figure 1b**).[24] Given this strong anisotropy, an important step in optimizing prospective PV devices relates to ordering the 1D $(Sb_4X_6)_n$ ribbons within the device such that they extend nominally perpendicular to the substrate for more facile charge transport through the device (**Figure 1c**).[27] An hypothesis underlying this idea is that, if the 1D ribbons are appropriately aligned within the absorber layer, then this system may, not only allow for facile charge transport during photoexcited carrier collection, but also reduce detrimental defects at the grain boundaries (given the weak van der Waals interactions that connect the 1D ribbons, which should minimize the presence of dangling bonds at grain boundaries and interfaces).

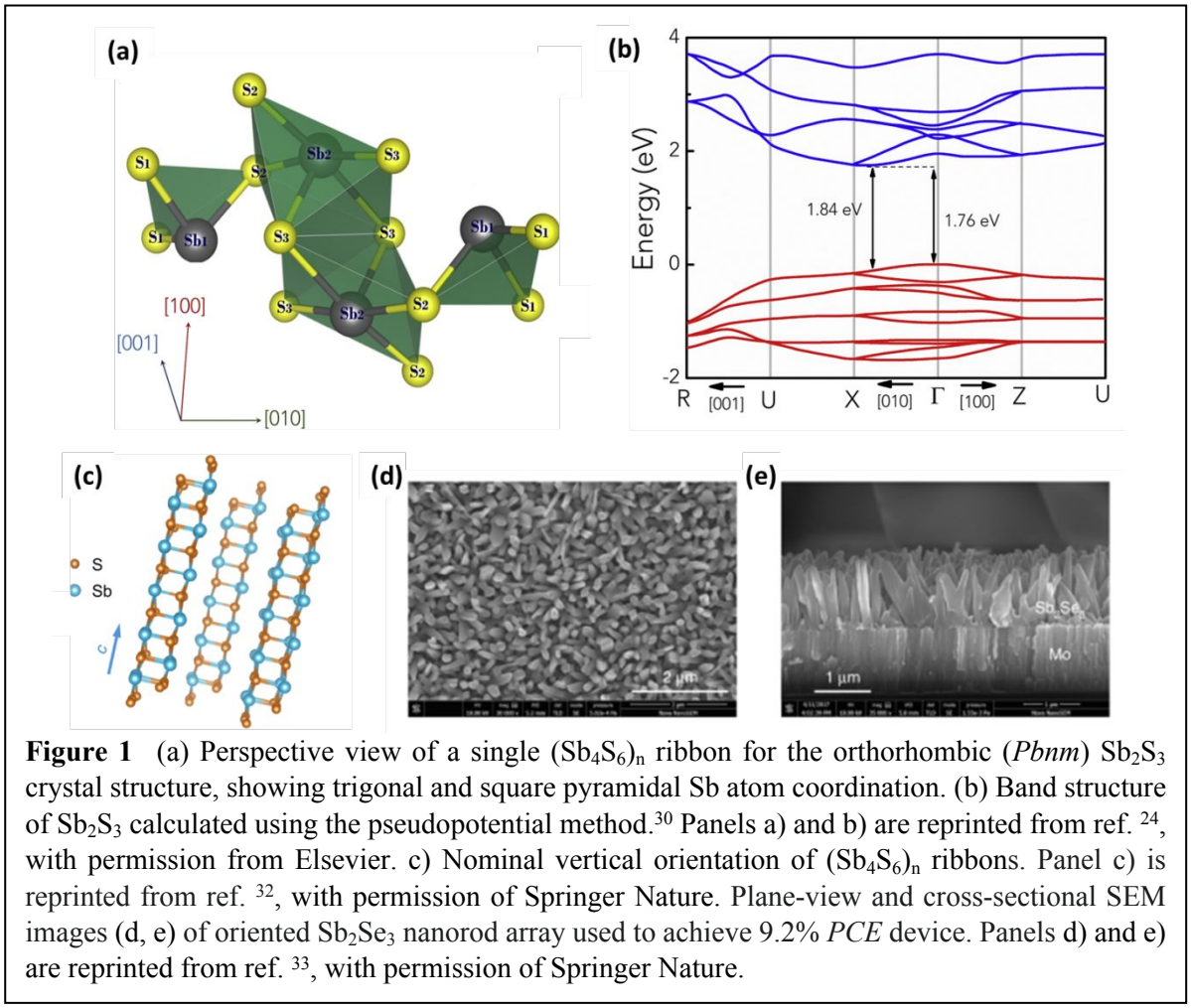

Figure 1 (a) Perspective view of a single $(Sb_4S_6)_n$ ribbon for the orthorhombic (*Pbnm*) Sb_2S_3 crystal structure, showing trigonal and square pyramidal Sb atom coordination. (b) Band structure of Sb_2S_3 calculated using the pseudopotential method.[30] Panels a) and b) are reprinted from ref. [24], with permission from Elsevier. c) Nominal vertical orientation of $(Sb_4S_6)_n$ ribbons. Panel c) is reprinted from ref. [32], with permission of Springer Nature. Plane-view and cross-sectional SEM images (d, e) of oriented Sb_2Se_3 nanorod array used to achieve 9.2% *PCE* device. Panels d) and e) are reprinted from ref. [33], with permission of Springer Nature.

Current highest performing Sb_2S_3 devices offer *PCE* = 7.5% (V_{oc} = 711 mV), based on a dye (i.e., Sb_2S_3)-sensitized solar cell device structure (i.e., F-doped SnO_2 (FTO)/compact TiO_2 blocking layer/mesoporous TiO_2/Sb_2S_3/PCPDTBT (PCBM)/Au; where PCPDTBT = poly(2,6-(4,4-bis-(2-ethylhexyl)-4*H*-cyclopenta[2,1-*b*;3,4-*b*′]dithiophene)-alt-4,7(2,1,3-benzothiadiazole)) and employing a post-deposition thioacetamide sulfurization treatment to minimize detrimental trap sites associated with S-deficiency and oxide formation for the Sb_2S_3.[28] Planar junction devices (i.e., FTO/ZnX_2-TiO_2/Sb_2S_3/Spiro-OMeTAD/Au; where spiro-OMeTAD = 2,2′,7,7′- tetrakis(N,N-di-p-methoxyphenylamine)-9,9′-spirobifluorene) have also reached >7% *PCE* (V_{oc} = 650 mV) using a zinc halide (X = I, Br, Cl) treatment of the TiO_2 electron transport layer (ETL) to improve the carrier mobility as well as Sb_2S_3 film morphology.[29] The detailed balance performance limit for a solar cell (AM 1.5G illumination) based on a 1.7 eV bandgap absorber offers V_{oc}=1402 mV, J_{sc}=22.46 mA/cm^2, *FF* = 91.0%, and *PCE* = 28.64%. These target characteristics highlight substantial shortfalls in current devices, especially as they relate to V_{oc}. Low carrier concentration levels (~10^{10}-10^{12} cm^{-3}) limit device efficiencies through increased series resistance and reduced built-in voltage; successful doping is found to be challenging due to the 1D structure and difficulties associated with heteroatom incorporation.[26] Another limitation relates to the recombination at the TiO_2/Sb_2S_3 interface and within the bulk absorber, arising from sulfur vacancies, oxidation products/defects at the absorber surface and from introduced impurity atoms.[31] A recent study has used deep-level transient spectroscopy (DLTS) to assign three types of deep level defects, depending on the detailed Sb_2S_3 film preparation condition and composition: a Sb-rich film displays two types of crucial defects, i.e., V_S and Sb_S, while the S-rich Sb_2S_3 film shows only one kind of critical defect, V_{Sb}.[32] The Sb interstitial, Sb_i, defect (especially for Sb-rich films) is found to have less significant impact on minority carrier lifetime, presumably due to the flexibility in the structure afforded by the 1D ribbons.

Best device performance levels for lower bandgap (and isostructural to Sb_2S_3) Sb_2Se_3-based devices have reached 9.2% *PCE*, using a Sb_2Se_3 nanorod array for the absorber (grown using a closed-space sublimation method) and a glass/Mo/$MoSe_2$/Sb_2Se_3/TiO_2/CdS/ZnO/Al:ZnO device structure.[33] A key aspect of this work is that the typical [221]-oriented Sb_2Se_3 films, with $[Sb_2Se_6]_n$ ribbons oriented at some tilt angle relative to the substrate, have been replaced by an array of Sb_2Se_3 nanorods with nominal [001]-orientation relative to the substrate (**Figure 1d, e**), providing for a larger expected electron diffusion length along this crystallographic direction. Additionally, the introduced TiO_2 layer serves to minimize Sb diffusion into the CdS layer during processing. By mixing S and Se in $Sb_2(S,Se)_3$ films, prepared using a hydrothermal deposition approach, the first devices with double-digit (certified 10.0%) *PCE* were achieved using a superstrate glass/FTO/CdS/$Sb_2(S,Se)_3$/Spiro-OMeTAD/Au device structure.[34] Best performance parameters are achieved for Se/(S+Se) ratio corresponding to 29%, which yields suitable absorber bandgap (1.57 eV), favorable $[Sb_4(S,Se)_6]_n$ ribbon orientation and reduced defect levels relative to other ratios. Minority carrier (hole) lifetimes of approximately 9 ns are determined for these films using transient absorption spectroscopy (TAS). This record was more recently improved to PCE = 10.7% in a device with the CdS layer replaced with a dual Zn(O,S)/CdS ETL and for which the $Sb_2(S,Se)_3$ absorber quality has been improved using a alkali metal fluoride (best efficiency achieved with NaF) solution post-treatment (SPT) (**Figure 2**).[35] Bandgap grading due to a SPT-modified S/Se

gradient is also expected to play a role in improved performance. An advantage of $Sb_2(S,Se)_3$ materials relates to the relatively high dielectric constant, k (e.g., k >15 for Sb_2Se_3 vs. k = 10 for CdTe), as higher dielectric constant allows for more effective screening of charged defects and reduced exciton binding energies in the semiconductor.[36,37] On the other hand, photoexcited carriers are readily self-trapped due to strong exciton-phonon coupling, which may contribute to large V_{oc} deficit in antimony chalcogenide solar cells.[36,38] As for Sb_2S_3, $Sb_2(S,Se)_3$ is subject to the impact of deep level defects (i.e., the materials are not "defect tolerant" and oxide impurities also play an important role) and addressing this issue represents a key direction for future materials/device improvement.[36]

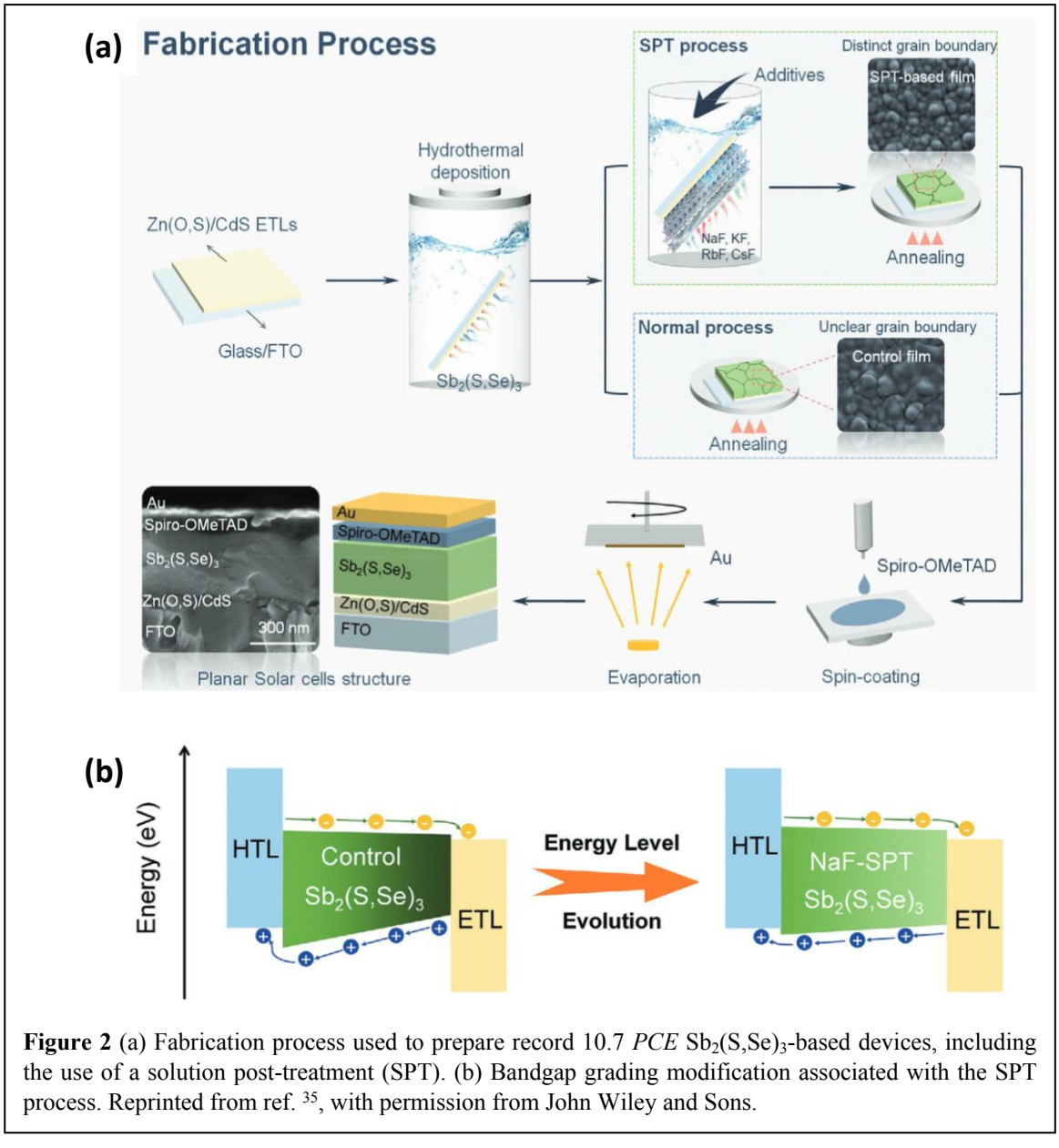

Figure 2 (a) Fabrication process used to prepare record 10.7 *PCE* $Sb_2(S,Se)_3$-based devices, including the use of a solution post-treatment (SPT). (b) Bandgap grading modification associated with the SPT process. Reprinted from ref. [35], with permission from John Wiley and Sons.

2.2 Sn(S,Se) / Ge(S,Se). Beyond Sb_2X_3 (X=S, Se), substantial research effort has focused on MX (M=Sn, Ge; X=S, Se) semiconductors (referred to as group IV-VI monochalcogenides). Prototypical SnS involves low-toxicity and earth-abundant Sn and S elements and generally crystallizes in an orthorhombic (*Pmcn*) structure displaying distinct SnS layers with weaker interlayer van der Waals bonding, thereby giving rise to significant crystallographic anisotropy (**Figure 3a, b**).[40,41] SnS is thermodynamically stable (found naturally as the mineral herzenbergite) and offers a near direct optical bandgap (i.e., indirect bandgap of 1.1 eV – 1.3 eV and direct bandgap of 1.4-1.5 eV), as well as a high absorption coefficient ($\alpha > 10^4$ -10^5 cm^{-1}), particularly at energies above 1.5 eV.[42] These properties allow for thinner absorbers to be used (< 1 μm thick) relative to commercialized CdTe and CIGS technologies.[12] Additionally, the relatively simple composition space for SnS allows for a range of facile vacuum- and solution-based film deposition approaches.[41] While initial SnS-based devices were limited to PCE ≈ 2%,[43,44] subsequent optimization steps for devices based on SnS films prepared by atomic layer deposition (ALD) included: 1) boosting grain size and increasing hole concentration (to ~$6x10^{15}$ cm^{-3}) using a post-deposition H_2S anneal (**Figure 3c-h**), 2) optimizing Zn(O,S):N buffer layer composition to improve band alignment at the absorber-buffer interface and doping level, and 3) introducing a SnO_2 SnS/Zn(O,S):N interface passivation layer through SnS film H_2O_2 vapor exposure and/or more directly using an ALD approach (**Figure 3i**). Such changes led to devices with V_{oc} of as high as 390 mV and PCE of as high as 4.6 % (with certified device performance parameters of V_{oc} = 372 mV, J_{sc} = 20.2 mA/cm^2, FF = 58% and PCE = 4.36%).[41]

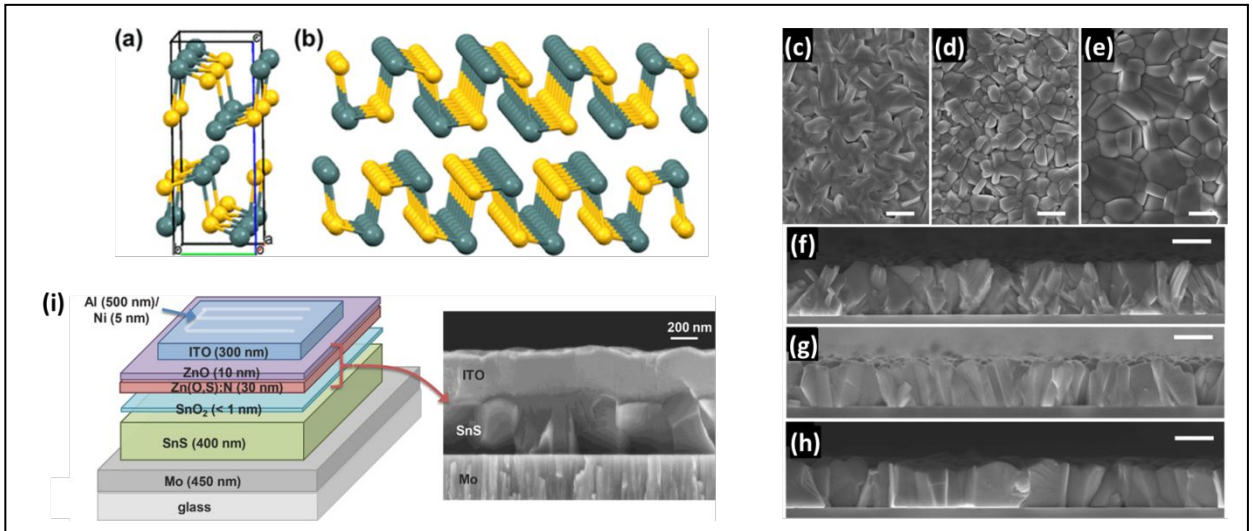

Figure 3 a) The orthorhombic unit cell of herzenbergite, tin(II) sulfide (space group *Pmcn*), which comprises corrugated layers of SnS held together by weak interlayer forces. (b) A SnS bilayer sheet viewed close to the [100] direction, i.e., parallel to the sheets. Panels a) and b) are reprinted with permission from ref. [39]. Copyright 2015 American Chemical Society. Plane-view and cross sectional SEM images of (c, f) as-deposited and annealed SnS films at 400 °C for 1 h in (d,g) N_2 and (e, h) H_2S atmospheres, highlighting enhancement in grain size with H_2S anneal. The scale bars denote 500 nm. (i) A schematic diagram of a 4.4% *PCE* SnS-based solar cell and cross-sectional SEM image of an actual cell with SnS annealed in H_2S. Panels c) - i) are reprinted from ref. [41], with permission from John Wiley and Sons.

Prospective concerns related to the slow absorber layer growth rate using ALD (perhaps contributing to higher fabrication costs) have more recently been addressed using a solution-based SnS absorber deposition approach, leading to uncertified *PCE* values of as high as 4.8% (V_{oc} = 330 mV, J_{sc} = 24.7 mA/cm^2, *FF* = 58.5%) in a FTO/TiO_2/SnS/Au device structure and after introducing a $SnCl_2$ post-treatment process.[45] Minority carrier lifetimes were measured in these films using time-resolved photoluminescence (PL), yielding values in the range of 5-10 ns. Further, relatively high-performance (*PCE* = 4.2%; V_{oc} = 346 mV, J_{sc} = 20.8 mA/cm^2, *FF* = 58.8%) devices have also been achieved using SnS films deposited by a vapor-transport-deposited (VTD) approach, similar to that used for commercial CdTe PV devices, and using a SnS/CdS junction.[46] High defect densities of order ~10^{17} cm^{-3} were measured for these films using admittance spectroscopy, consistent with the expectation (given low V_{oc}) of the devices being severely limited by recombination. Homojunction devices employing n-type SnS single crystal and p-type SnS overlayers have also recently been prepared, but so far have not yielded higher performance parameters than heterojunction analogs.[47]

Overall, despite a theoretical maximum efficiency of 32%,[41] the current experimental *PCE* values of <5% attest to the challenges of optimizing the SnS device technology. Important challenges for such optimization, beyond those mentioned above, likely involve achieving phase purity in the targeted SnS films (e.g., avoiding formation of Sn_2S_3 and SnS_2 secondary phases), minimizing interface and bulk sulfur/tin vacancy (V_S/V_{Sn}) and Sn^{4+}-related defects, and controlling atomic diffusion and ordering at the absorber-buffer interface.[41,45,46,48] Importantly, unlike CdTe, with isotropic crystal structure and for which Cd has a well-defined 2+ oxidation state, SnS has additional complications related to the readily accessible 4+ oxidation state (i.e., allowing for multivalency), the anisotropic crystal structure and associated electronic properties (i.e., requiring therefore a preferred film orientation for best device performance), as well as prospects for different competing crystal structure types (i.e., orthorhombic vs. cubic) even within the SnS stoichiometry, which each contribute to rendering device structure optimization more challenging than for CdTe.[12]

Recent work extends beyond SnS to systems including GeSe, which offers an indirect 1.1 eV bandgap (with a direct transition of 1.2 eV), p-type majority carrier mobility of as high as 129 cm^2/V-s, and structural/optical characteristics similar to SnS, with minority carrier lifetime measured by transient absorption spectroscopy (TAS) of order 10 ns.[49] Further, band structure calculations point to the possibility that bulk GeSe may offer "defect tolerant" properties, similar to the case of halide perovskites, due to anti-bonding character at the valence band maximum (VBM).[50] Device *PCE*s of as high as 5.5% (V_{oc} = 360 mV, J_{sc} = 26.6 mA cm^{-2}, and *FF* = 57%; certified *PCE* is 5.2%) have been achieved using a Sb_2Se_3 surface passivation layer between the CdS and GeSe layers to reduce interfacial recombination; this work additionally points to the need to further reduce surface recombination.[50,51] As for SnS, recent work on GeSe materials seeks control over the preferred crystallographic orientation of the absorber films, with a target of the 2D Ge-Se layers being oriented nominally perpendicular to the plane of the junction for most effective charge transport, coupled with improvement in the band offsets at the absorber/charge transport layer interfaces.[52] SnSe devices based on VTD-deposited absorber layers have also been

recently explored, yielding 2.5% *PCE*.[53] Notably, selenium (~0.05 ppm) is less abundant in the earth's crust than sulfur (~420 ppm),[12] which points to the fact that these Se-based materials are perhaps less likely to be compatible with multiple TW-scale deployment.

2.3 Selenium (Se). Despite the reduce chemical abundance, if chemical complexity presages film processing and defect control challenges, then polycrystalline Se, an *elemental* p-type semiconductor with a direct bandgap of 1.8-2.0 eV (depending on processing), provides interesting opportunities for PV, particularly as the top cell in a tandem device.[54-61] With a trigonal structure comprised of hexagonally packed helical chains of Se atoms (**Figure 4a**),[62] crystalline selenium offers a high absorption coefficient ($\alpha > 10^5$ cm^{-1} for wavelengths below ~600 nm)[55] and facile low-temperature processing (i.e., Se melts at ~220 ˚C and may be readily evaporated or solution processed). Early superstrate glass/ITO/Se(4 μm)/Pt solar cells, incorporating a 1.5 – 10 nm-thick Te interlayer to improve the bonding at the ITO-Se interface, offered efficiencies of up to 2.5 % (AM 1 illumination).[56] The *PCE* was improved to 5% (AM 1.5 illumination) using a glass/ITO/TiO_2 (50 nm)/Se (2 μm; E_g = 1.95 eV)/Au structure.[57] Incorporation of the n-type TiO_2 layer in the device (still employing the Te adhesion layer) was found to improve V_{oc} to 884 mV. More recent devices added an ~20-nm-thick MoO_x high work function hole selective layer between the Se and Au back contact to reduce recombination, employed a substantially thinner Se absorber (100 nm) to enhance the effect of the back surface field, and substituted a tunable bandgap $Zn_xMg_{1-x}O$ n-type buffer for TiO_2, leading to a V_{oc} of 969 mV and *PCE* of 6.5%, the current record for this technology (**Figure 4b, c**).[58]

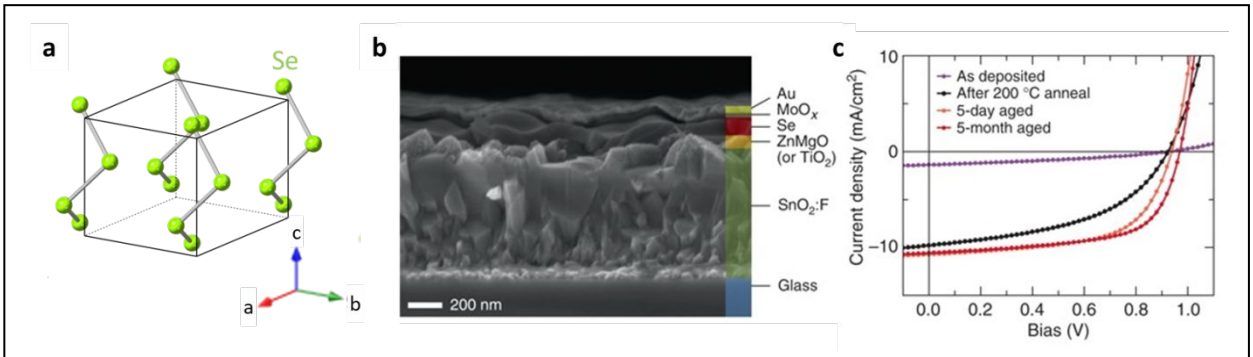

Figure 4 a) Crystal structure of trigonal ($P3_121$) Se. Crystallographic data is from ref. [62]. b) Cross section scanning electron microscopy of the glass/SnO_2:F/ZnMgO buffer/Se/MoO_x/Au device structure used for the record 6.5% *PCE* Se-based device.[58] A Te adhesion layer is employed at the n-type buffer/Se interface. c) Illuminated *J–V* plots of devices with as-deposited (amorphous), annealed at 200 ˚C (crystallized), 5-day aged after annealing, and 5-month aged after annealing Se. Panels b) and c) are reprinted with permission from ref. [58], with permission of Springer Nature.

The as-evaporated amorphous Se films require annealing at temperatures of ~200 ˚C for several minutes to induce trigonal phase crystallization (**Figure 4c**). Device performance remains stable and in fact increases with time up to at least 5 months.[58] Hole density (2.8×10^{12} cm^{-3}) and mobility (0.46 cm^2 V^{-1} s^{-1}) values were established by AC Hall effect for Se films employed in the record device study and these low values likely serve to limit device performance, along with presumed short minority carrier lifetime. Recent work has focused on trying to invert high-performance device structures from superstrate to substrate configuration (a preferred geometry

for tandem use), with an appropriate n-type heterojunction partner and without introducing damage to the Se absorber during the buffer deposition.[59] A 3.9% PCE inverted p-i-n device comprising poly(3,4-ethylenedioxythiophene) polystyrene sulfonate (PEDOT:PSS)/Se/phenyl-C61-butyric acid methyl ester (PCBM) layers has recently been demonstrated.[60] In this structure, PCBM both serves as an ETL and as a blocking layer to inhibit reaction between Se and the top Ag contact used in the device. Given the significantly anisotropic (i.e., 1D) nature of the trigonal Se crystal structure, film processing enhancements to impact film preferred crystallographic orientation are being developed to further improve device performance (as for 1D Sb_2Se_3, see Section 2.1).[61] Another direction of current interest relates to tuning of the Se absorber bandgap to lower value, for example by alloying with Te.[63,64] Further, there remains a need to understand and engineer recombination pathways and doping (Fermi level control) in this system.

2.4 CZTS and CBTS. Shifting in a different direction from the simplicity of the monoatomic and binary chalcogenide semiconductors, an alternative direction of research focuses on introducing additional chemical complexity to allow for more tunability. For example, in established CIGS technology (i.e., using the dual-alloying approach $Cu(In,Ga)(S,Se)_2$), tuning In:Ga and S;Se simultaneously allows for bandgap tailoring or grading, as well as independently varying the absolute band positions, which can be useful for optimization of conduction/valence band offsets and for maximizing the electric fields that are present in the device structures.[65,66] While CIGS exists as a commercialized technology, concerns remain regarding the scalability of the technology given complexity and reproducibility of the film deposition approach, as well as related to the elemental abundance and cost of In and Ga. Given these concerns, interest has focused on the kesterite $Cu_2ZnSn(S,Se)_4$ (CZTS) as a prospective earth-abundant and relatively low-toxicity drop-in replacement for CIGS.[67,68] The kesterite structure type (**Figure 5a**) shares the 3D-connected tetrahedral cation/anion coordination with zinc-blende and chalcopyrite structures. However, the associated cation ordering leads to a distinct tetragonal structure type.

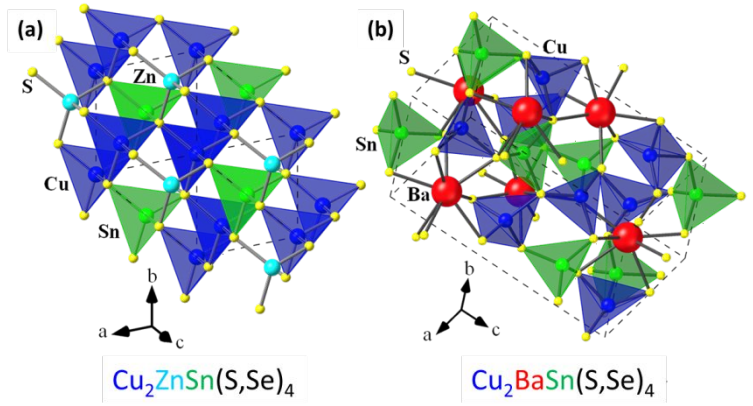

Figure 5 Combined ball-and-stick and polyhedral representation of the a) CZTS (kesterite) and b) CBTSSe-type structures. Atom colors are reflected in the compound labels.

Since first observation of PV effects from prototype devices by Ito and Nakazawa[69] in 1988, CZTS solar cells have shown notable improvements, achieving a record *PCE* of 12.6 % (V_{oc} = 513.4 mV, J_{sc} = 35.2 mA, *FF* = 69.8 %) by Wang *et al.*[70] in 2014 using a substrate-type glass/Mo/CZTS/CdS/i-ZnO/ITO device structure and an appropriate S/Se ratio to achieve E_g = 1.13 eV. A recent (2022) report has yielded *PCE* = 13.6% (V_{oc} = 537.5 mV, J_{sc} = 36.2 mA, *FF* = 69.8 %), although the details of bandgap and how performance has been improved are pending

publication of results.[71] The *PCE* value of 12.6 (or more recently 13.6) % is still far less than the record *PCE* for CIGS (23.4 %) and CdTe (22.1 %) analogs.[71] A key limiting factor for CZTS solar cells relates to low open-circuit voltage (V_{OC}).[72,73] The V_{OC} deficit in turn correlates, at least in part, with the small energy cost for the exchange among Cu and Zn atoms in the lattice due to their similar size, coordination, and chemical valence.[74-77] The similarities between the two atoms result in formation of a high density of detrimental anti-site defects and defect-clusters in the CZTS lattice and introduce band tailing (**Figure 6a, b**), which can limit V_{OC} and efficiency of the CZTS solar cells.[78-80] Given the similar sizes and coordination for Cu, Zn and Sn, other permutations of anti-site defects and related defect clusters (e.g., Cu_{Sn}, Zn_{Sn}, Sn_{Zn}, Cu_{Zn}+Sn_{Zn}) also make important contributions to the V_{OC} deficit in the form of band tailing and/or deep defects.[75,81,82]

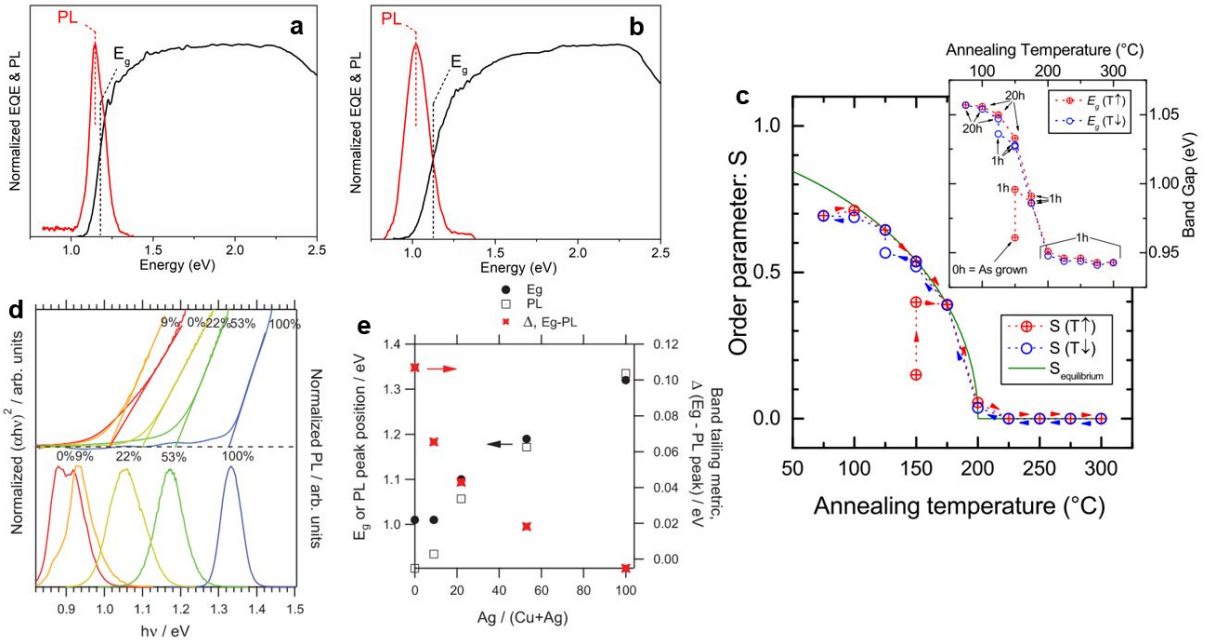

Figure 6 EQE and PL spectra for (a) CIGS, and (b) CZTS solar cells. CZTS shows a broader PL peak and large deviation between E_g and PL peak positions, reflecting a higher degree of band tailing in this system. Data for plots in panels (a) and (b) are from ref. [78]. (c) Calculated evolution of the order parameter (S) during successive annealing treatments of CZTS films. The inset illustrates the evolution of band gap (E_g) for the corresponding sequence. The labels shown in the inset indicate annealing time. Panel (c) is reprinted from ref. [83], with the permission of AIP Publishing. (d) $(\alpha h\nu)^2$ and PL spectra, (e) E_g and PL peak positions (and resultant band tailing metric) for $(Cu,Ag)_2ZnSnSe_4$ films with different Ag/(Ag+Cu) composition ratios. Panels (d) and (e) are reprinted from ref. [84], with the permission of John Wiley and Sons.

To suppress disorder and associated band tailing, two primary strategies have been implemented: 1) adjustment of post-annealing conditions,[83,85-88] and 2) full or partial substitution of elements with another species. The first approach focuses on changing the level of cation order in the crystal lattice, which is reflected by order parameter (S) calculated from the Vineyard model,[89] by adjusting post-annealing conditions such as temperature and time (**Figure 6c**).

However, the observed reduction in band tailing, achieved with low-temperature post-annealing, has been limited,[88] meaning that such treatment has not adequately mitigated band tailing and V_{OC} deficit. The second approach involves substituting Cu or Zn with another element that gives more substantial ionic size mismatch to minimize anti-site related lattice disorder within the kesterite or related stannite structures. This approach has introduced $(Cu,Ag)_2ZnSn(S,Se)_4$ and $Cu_2MSn(S,Se)_4$ (M = Cd, Mn, Fe, Co) systems.[84,90-95] Among these, compounds with alloyed Ag or Cd have been reported to successfully reduce the band tailing (**Figure 6d, e**) and mitigate the V_{OC} deficit to some extent.[84,90-92] However, there are also several limitations for this pathway, such as toxicity of Cd, semiconductor carrier-type inversion induced by Ag,[84,90] and multiple-charge states of the transition metals (Mn, Fe, Co), which may introduce deep trap states.[96-98] Cation/anion substitution may also be used for targeted bandgap modification and grading, as in the case of Ag or Ge substitution for Cu and Sn, respectively.[99,100] Bandgap grading can be used to selectively tailor the fields at the front and back of the device in an effort to improve recombination characteristics.

Another approach for reducing disorder relates to substituting Zn with a significantly larger and chemically more differentiated group-2 elements such as Ba, which introduces the $Cu_2BaSnS_{4-x}Se_x$ (CBTSSe) system. Barium (Ba^{2+} : 1.42 Å) not only has a larger ionic size than Cu (Cu^{+} : 0.60 Å),[101] but also has a distinct 8-fold coordination environment in the CBTSSe structure relative to tetrahedrally-coordinated Zn in CZTS (**Figure 5b**).[102] Such dissimilarities between Cu and Ba are predicted to yield significantly higher formation energies for corresponding anti-site defects and suppress associated band tailing.[103] Because CBTSSe also consists of only earth-abundant, less toxic metals, as for CZTS, work on this system has motivated studies on the film deposition processes based on both solution-[104] and vacuum-based techniques,[105-107] as well as their PV[105,106] and water electrolysis[104,107] applications. Progress for CBTSSe-related PVs are discussed in more detail in Sections 3 and 4.

2.5 $CuPbSbS_3$ (bournonite). As another example of multinary chalcogenide, bournonite has recently been proposed as a stable photoferroic absorber,[108] with potential for an enhanced minority carrier lifetime due to a spin splitting in the conduction band (leading to a "quasi-direct" or "nearly direct" bandgap), arising from the non-centrosymmetric orthorhombic crystal structure (**Figure 7a**) and significant spin-orbit coupling (SOC) due to the heavy Pb atom. $CuPbSbS_3$ offers strong absorption and a bandgap of ~1.3 eV, within the ideal range for a single junction PV device. While both n-type and p-type semiconducting character have been reported,[109] recent results on carefully prepared solution-processed films point to weakly p-type character under S-rich fabrication conditions.[110] This study also used density functional theory (DFT) to predict a defect tolerant character for the bournonite films (V_{Pb}, V_{Cu}, Cu_{Pb}, Pb_{Sb}, Cu_i and Sb_{Pb} show low formation energy and are shallow donors/acceptors), like the case for the Pb-based halide perovskites. Recent devices based on superstrate glass/ITO/CdS/$CuPbSbS_3$/Spiro-OMeTAD/Au and glass/FTO/TiO_2/$CuPbSbS_3$/Spiro-OMeTAD/Au (**Figure 7b, c**) architectures yield *PCE* values of 2.23% and 2.65%, respectively.[110,111] In the latter record device, the V_{oc} of 572 mV still shows a substantial deficiency, given an E_g = 1.3 eV. Recent work has focused on the challenge of using first-principles calculations to predict an appropriate heterojunction partner for bournonite (e.g., SnS_2 is suggested as a suitable option for p-type bournonite).[109] Clearly, a significant amount of

research is still required to better understand the fundamental semiconductor characteristics (e.g., majority carrier properties, energy band positions relative to prospective charge transport layers, minority carrier lifetime and diffusion length, surface/bulk defect properties) and interface characteristics in bournonite-related films and device structures prior to allowing for firm conclusions regarding the suitability of this system for practical PV application.[109] The bournonite system also has the issue of toxicity based on lead (Pb) use, leading to the question of whether Pb can be partially or fully replaced by other less toxic metals.

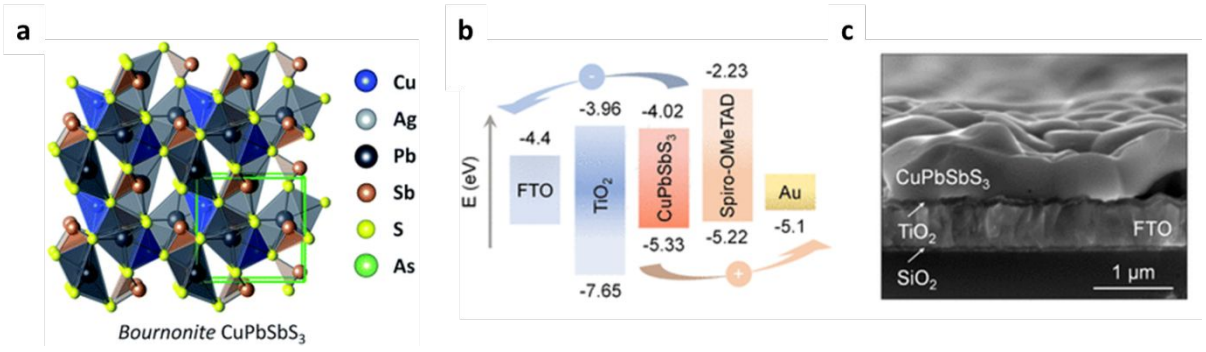

Figure 7 a) 3D extended crystal structure ($Pmn2_1$) of bournonite. Panel a) is reprinted from ref. [108], with permission from the Royal Society of Chemistry. b) Energy band diagram for record *PCE* = 2.65% bournonite PV device. c) SEM image of solution-processed bournonite film cross section. b) and c) are reprinted with permission from ref. [111]. Copyright 2021 American Chemical Society.

2.6 Beyond chalcogenides. While the current review focuses on chalcogenides, no review of prospective TFPV absorbers would be complete without mentioning halide-based perovskites, which since their first application in solar cells[112] have blossomed into a massive materials and device community research effort, with many thousands of articles being published per year (several recent reviews are found in refs [113-115]). A clear distinction for the halide perovskite semiconductors relates to the very attractive V_{oc} values—e.g., a record device offers V_{oc} = 1179 mV,[71] which is close to the fundamental limit of 1215 mV[116] for a single junction device with E_g = 1.5 eV under AM1.5 illumination (note, however, that the exact bandgap of the record absorber was not provided), leading to the current record *PCE* = 25.7 %.[71] Such outstanding performance characteristics arise from extremely high optical absorption over the relevant wavelength range, small effective masses for electrons/holes, dominant point defects that only yield shallow levels (i.e., the compounds are considered "defect resistant"), and almost completely benign grain boundaries with respect to recombination, which in turn follow from the Pb lone pair *6s* orbitals and perovskite structural symmetry.[117] These desirable properties, coupled with multiple facile low-cost processing options,[118] render perovskites an extremely compelling area of current TFPV research. Nevertheless, the most successful halide perovskite absorbers are based on the heavy metal lead (Pb) and these absorbers currently do not offer sufficient operational stability for commercialization. Circling back to the chalcogenide theme, non-Pb chalcogenide-based perovskite absorbers (e.g., $BaZrS_3$) have also recently been proposed for use in PV devices,

although no devices with appreciable *PCE* have been demonstrated.[119,120] Finally, another interesting non-chalcogenide direction of recent interest for TFPV can be found in the nitride/phosphide families (e.g., Zn_3P_2, $ZnSnP_2$ and $ZnSnN_2$),[121-123] with power conversion efficiencies currently being limited to ~6% for Zn_3P_2.[124]

3. CBTSSe as a Model System

The multinary CBTSSe-related absorbers introduced in Section 2.4 represent a focal area of particular interest for the authors and we will therefore devote the remainder of Sections 3 and 4 to these systems. An initial study on CBTSSe as a potential PV material was conducted by Hong et al.,[103] in which the authors investigated band structures and partial densities of states for Cu_2BaSnS_4 (CBTS) as well as isostructural Cu_2SrSnS_4 (CSTS), using DFT calculations. The authors found that both CBTS and CSTS have indirect bandgaps of ~1.77 eV, with conduction band minimum (CBM) near the Γ point and VBM at the A point. However, the difference between indirect and direct bandgaps is only ~0.02 eV and ~0.01 eV, respectively, smaller than the thermal energy at room temperature ($k_BT \approx 0.026$ eV) and indicating that these compounds can be considered as "quasidirect" bandgap materials at typical temperatures employed in PV devices. The VBM of both compounds consists of anti-bonding states from Cu 3d and S 3p orbitals, while CBM mainly originates from Sn 5s with small contribution from S 3p and 3s states (i.e., very little contribution from Sr and Ba at the band edges and analogous to CZTS). The bandgap of $Cu_2BaSnS_{4-x}Se_x$ (CBTSSe; $x = 0 – 4$) was also calculated. Although the calculated bandgap for CBTS (1.77 eV) is larger than optimal for single junction PV,[125] incorporation of Se reduces the bandgap (**Figure 8a**) to 1.28 eV for $Cu_2BaSnSe_4$, assuming stability of the trigonal ($P3_1$) structure throughout the composition range. The same group also examined intrinsic defect properties of CBTS, yielding insights into intrinsic film properties and favorable synthesis conditions in terms of solar cell performance. As expected, Ba_{Cu} and Cu_{Ba} defects have dramatically higher formation energies than Zn_{Cu} and Cu_{Zn} in CZTS, indicating that substituting Zn with Ba suppresses formation of anti-site defects and disordering. The authors also mention that the defects with low formation energies in CBTS mostly form shallow-levels rather than deep-levels, suggesting good recombination properties for CBTS. Among these defects, V_{Cu} and Cu_{Ba} are shallow acceptors, while Cu_i and Ba_{Cu} are shallow donors (**Figure 8b, c**). All other defects are expected to create deep levels. Also, V_{Cu} acceptors and Cu_i donors have the lowest formation energies regardless of growth conditions, with V_S as the dominant deep donor defect predicted to be detrimental for PV performance. Under Cu-poor and S-rich condition, the Fermi-level is expected to pin close to the VBM, which results in p-type conductivity with minimized V_S deep-level formation. Thus, Cu-poor and S-rich condition is expected to be the optimal growth condition for CBTS.

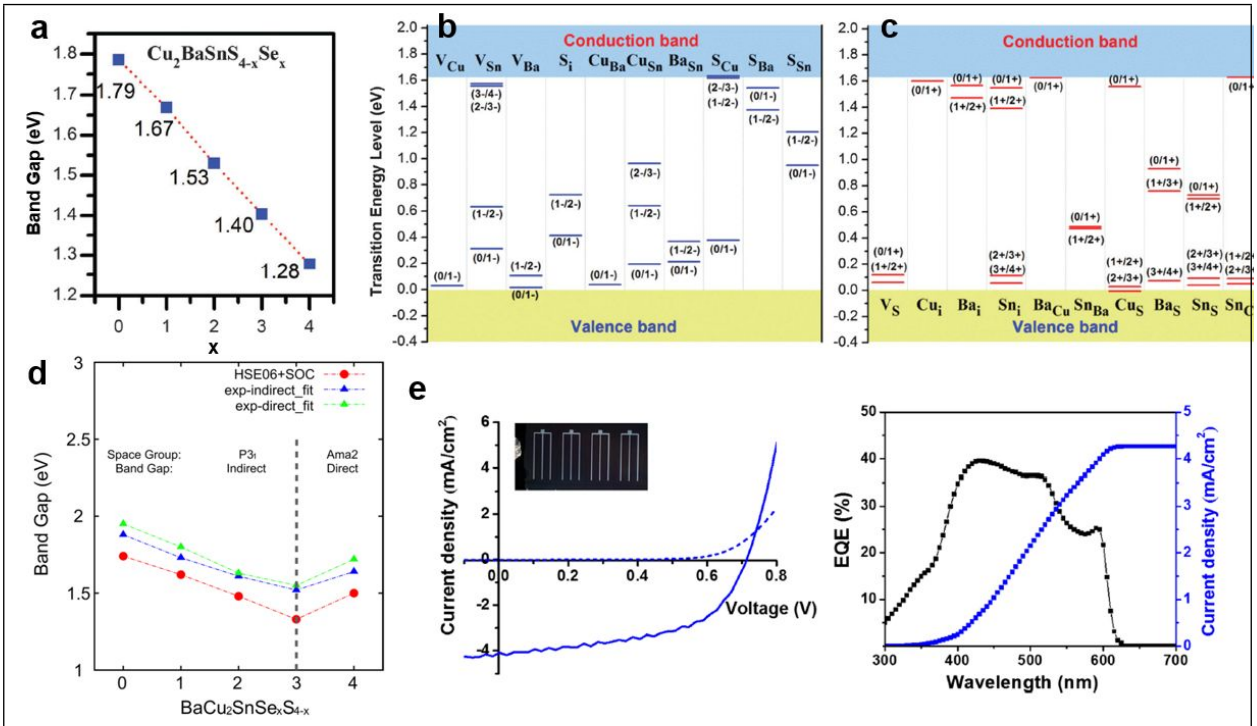

Figure 8 (a) HSE-calculated bandgap values, assuming CBTSSe maintains the trigonal ($P3_1$) crystal structure regardless of *x*. Calculated transition energy levels of (b) acceptor-like and (c) donor-like defects in CBTS. Panels (a) and (b) are reprinted from ref. [103], with permission from the Royal Society of Chemistry. (d) Evolution of experimental and HSE-calculated bandgap values with increasing Se content in the CBTSSe ($0 \leq x \leq 4$) solid solution, highlighting the structural transition to *Ama*2 for $x > 3$. (e) Light and dark J-V curves (inset shows an optical image of four adjacent PV devices) and EQE spectrum of the same CBTS (pure sulfide) solar cell (black line) and integrated photocurrent density under AM 1.5G illumination (blue line). Panels (d) and (e) are reprinted with permission from ref. [106]. Copyright 2016 American Chemical Society.

The aforementioned theoretical prediction by Hong *et al.,*[103] assumes that CBTSSe retains the $P3_1$ crystal structure regardless of S/Se ratio ($0 \leq x \leq 4$). However, experimental work by Shin *et al.,*[106] revealed that CBTSSe can have either trigonal ($P3_1$) or orthorhombic ($Ama2$) structure type for $0 \leq x \leq 3$ and $x > 3$ regimes, respectively (**Figure 8d**). The orthorhombic phase leads to higher bandgap ($E_g > 1.6$ eV) than the trigonal phase with $x = 3$ ($E_g = \sim 1.55$ eV), implying that CBTSSe bandgap tunability is limited (on the low-value end) to 1.55 eV and that, for single junction solar cells under AM1.5 illumination, $x = 3$ is likely the optimal composition.[125] The first solar cell devices based on co-sputtered CBTS solar absorbers were demonstrated based on a conventional device structure consisting of Mo back contact, CdS buffer, and i-ZnO/ITO window layers,[106] showing a maximum *PCE* of ~1.6 % (**Figure 8e**). Later, Shin et al.,[105] also demonstrated CBTSSe films based on sputtered Cu–BaS–Sn precursor layers and sequential reaction steps consisting of sulfurization followed by selenization to adjust the S/Se ratio in the final films. CBTSSe films with $x \approx 3$ were utilized as the absorber layer for solar cells, and the devices showed noticeable improvement in *PCE*, initially from 2.2 % up to 5.2 % after a post-deposition annealing step under air at 200 °C for 3 min. The authors attributed the performance improvement to the passivation of grain boundaries via oxidation, which improves recombination properties of the CBTSSe layer, as

supported by improvement in PL intensity of the CBTSSe layer after such treatment.[105] Similar behavior and improvement with annealing have also been reported for CZTS films.[126]

Later, overall optoelectronic properties (**Figure 9**) for CBTSSe films ($x \approx 3$; $E_g = 1.59$ eV) prepared using a solution-based method were examined by Teymur *et al*.[127] Photoconductivity transient evaluation was conducted using optical pump terahertz probe spectroscopy (OPTP) with variable excitation wavelengths (400 nm or 800 nm). CBTSSe exhibits two distinct lifetime components (~18–75 ps and ~2.5 ns), as shown in **Figure 9c**, attributed to surface and bulk recombination, respectively. The latter lifetime is comparable to the bulk lifetime measured for CZTS using a similar approach (~4.4 ns).[128] The relatively short carrier lifetime indicates the continued (despite substantial reduction in band tailing, as mentioned earlier) presence of harmful deep-level defects. The intragrain sum mobility determined from OPTP, ~140 $cm^2/V{\cdot}s$, is also comparable to values for CZTS (109 $cm^2/V{\cdot}s$ – 135 $cm^2/V{\cdot}s$).[128] Defect levels in CBTSSe films were also examined using temperature- and excitation-dependent PL (**Figure 9d**). The PL spectra reveal a dominant defect emission at 1.50 eV and another weaker emission at 1.15 eV, which can be attributed to shallow- and deep-acceptor levels, respectively. The detected deep acceptor-level may account for, at least in part, the limited minority carrier lifetime (< 10 ns). Notably, the above

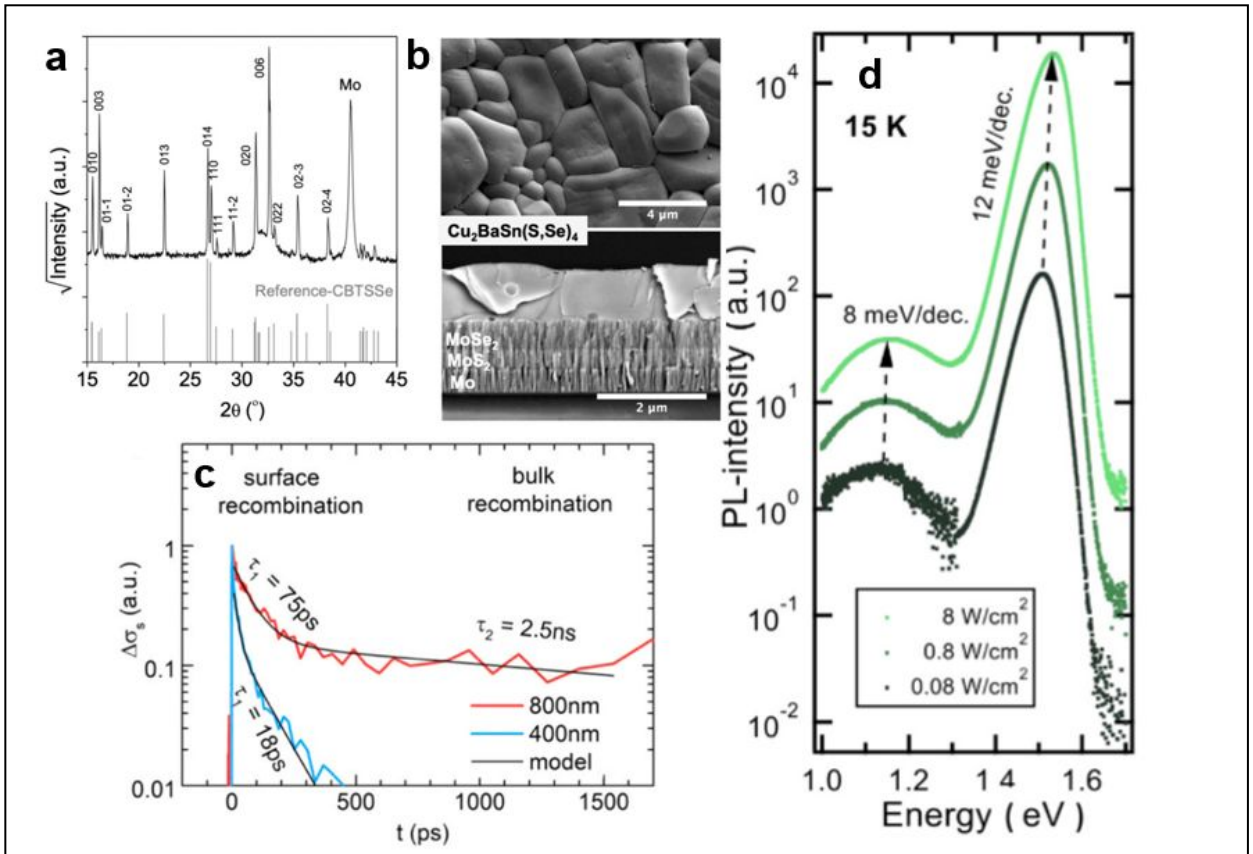

Figure 9 (a) X-ray diffraction pattern and (b) surface and cross-sectional SEM images of a representative solution-processed CBTSSe film. (c) Transient photoinduced sheet conductivity, $\Delta\sigma_s$, after an excitation with 400 nm and 800 nm illumination. (d) Excitation-dependent PL spectra for the CBTSSe film at low temperature (15 K) showing two defect emission peaks at ~1.5 eV and ~1.1 eV. Reprinted from ref. [127], with permission from Elsevier.

issues with deep levels are also present in solution-processed CBTS ($x \approx 0$; $E_g = 2.1$ eV) films.[129] Furthermore, the electron affinity (EA) for CBTSSe, determined by UPS/IPES measurement, is 3.52 eV, a noticeably lower value than for CdS (4.15 eV). The measured EA value implies that CBTSSe/CdS heterojunctions likely involve a large cliff-type conduction band offset (CBO << 0 eV), which is detrimental in terms of interface recombination.[130] These results indicate that typical CBTSSe solar cells with CdS buffer layers are not only limited by the bulk properties for CBTSSe (i.e., short bulk minority carrier lifetime), but also by the usage of the standard CdS buffer layer, which leads to a high degree of interface recombination and limited V_{OC}. This finding also agrees with theoretical investigation of band alignment between CBTS (as well as other Cu_2-*II*-*IV*-X_4 compounds) and CdS using first-principles calculations,[131] which shows that heterojunctions between CBTS and CdS form undesirable large negative CBO values.

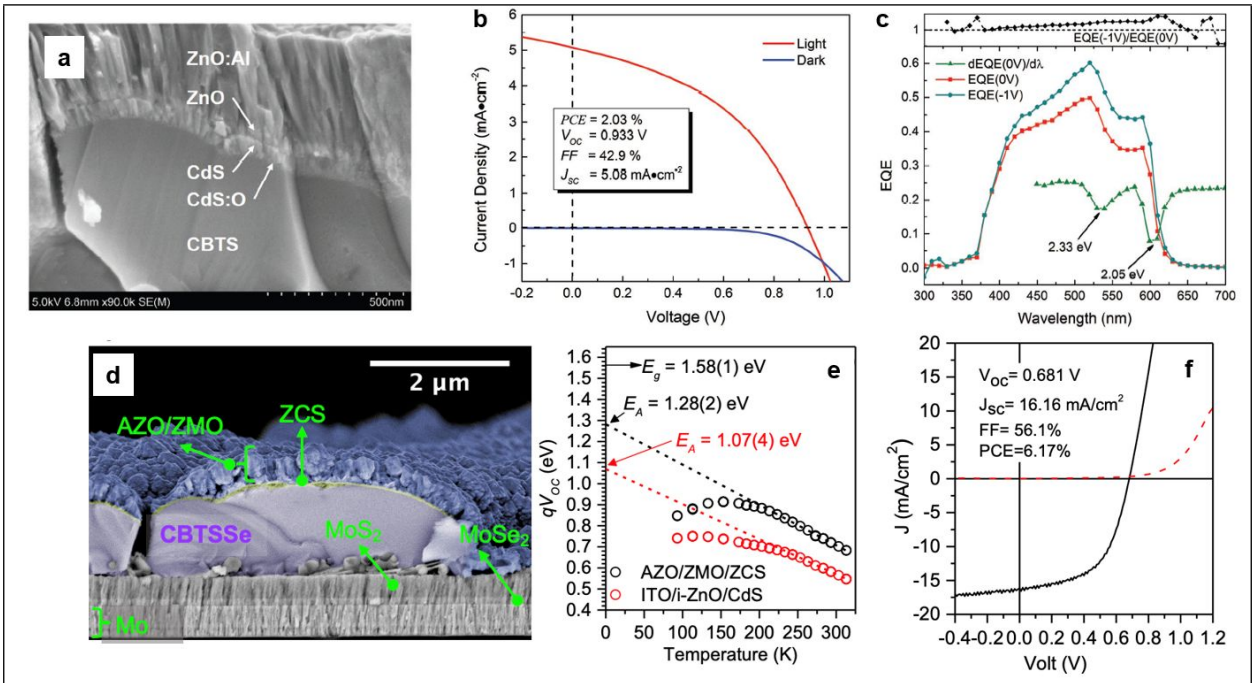

Figure 10 (a) Cross-sectional SEM of a finished CBTS PV with a configuration glass/FTO/CBTS/CdS:O/CdS /ZnO/ZnO:Al, (b) light and dark *J–V* curves, and (c) 0 and −1 V biased EQE, dEQE/dλ *vs.* wavelength curves for associated devices. Panels (a-c) are reprinted from ref. [132], with the permission of John Wiley and Sons. d) cross-section SEM of current record device with glass/Mo/Mo(S,Se)$_2$/CBTSSe/$Zn_{0.15}Cd_{0.85}$/$Zn_{0.7}Mg_{0.3}$O/ZnO:Al structure. (e) Temperature *vs.* q*Voc* plot, where linear extrapolation to the y-axis corresponds to the activation energy of the dominant recombination pathway (E_A); (f) light and dark *J-V* of the record device without anti-reflective coating. Panels (d-f) are reprinted with permission from ref. [133].

So far, only two experimental studies have addressed optimizing the CBO between the absorber and buffer layers for CBTS and CBTSSe solar cells. Ge *et al*.[132] showed that CBTS forms a negative CBO with CdS (CBO < 0 eV) using a flat-band potential technique. To move the CBM of the buffer layer upwards, the authors added O_2 in the Ar gas during sputter deposition of CdS to form a CdS:O buffer (cross-section image shown in **Figure 10a**). Use of CdS:O leads to improvement in V_{oc}, consistent with reduced interface recombination at the heterojunction. However, higher O_2 content (5 %) causes noticeable reduction of J_{SC} and *FF*, implying a large

spike type CBO (CBO > 0 eV) at the CBTSSe/CdS:O junction.[132] The maximum PCE of 2.03% is achieved using 3% O_2 content, combined with further replacing i-ZnO with CdS layer to improve *FF* (**Figure 10b, c**).[132] A second more recent work by Teymur *et al.*[133] based on solution-processed CBTSSe films, fully substituted the front contact stack (i.e., CdS/i-ZnO/ITO) with lower electron affinity counterparts (i.e., $Cd_{0.85}Zn_{0.15}S/Zn_{0.7}Mg_{0.3}O$/ZnO:Al (**Figure 10d**). The authors prepared the 40 nm – 50 nm thick $Cd_{0.85}Zn_{0.15}S$ layers using a sequential ionic layer adsorption and reaction (SILAR) method, which involves sequential dipping of substrates into cationic and anionic solutions for 30 cycles to achieve the targeted thickness. According to XPS measurements, the CBOs for CBTSSe/CdS and CBTSSe/$Cd_{0.85}Zn_{0.15}S$ heterojunctions are –0.46 eV, and –0.19 eV, respectively, indicating that $Cd_{0.85}Zn_{0.15}S$ provides a more favorable band alignment (i.e., less cliff-type) with CBTSSe ($x \approx 3$). This improvement in band alignment upon substituting the new front stack also yields an increase in the activation energy for the dominant recombination process (E_A) from 1.07 eV to 1.28 eV (i.e., closer to the bandgap value of 1.59 eV for the absorber), as estimated from the temperature-dependent V_{OC} plot (**Figure 10e**).[133] The new device structure enables a new record *PCE* of 6.2 % (**Figure 10f**; *PCE* = 6.5% with anti-reflection coating) for CBTSSe-related absorbers and confirms that one of the major challenges for device performance in such PVs is related to the energy band offsets for adjacent layers. Based on the new results, the current generation CBTSSe devices appear to still be limited by: 1) a lower doping level for the buffer (i.e., as Zn content increases in $Cd_{1-x}Zn_xS$), 2) a continued cliff-type CBO at the CBTSSe/$Cd_{0.85}Zn_{0.15}S$ heterojunction, which can cause elevated interface recombination, 3) still non-optimal electron affinity and work function offsets for the window (AZO/ZMO) layers, 4) an overall high series resistance for the devices, which limits the *FF*, and 5) persistent issues with elevated bulk recombination. According to a SCAPS-1D simulation (without considering parasitic resistance effects), CBTSSe solar cells can be further improved up to *PCE* ≈ 10 % once the properties of adjacent layers are optimized, even assuming the current non-ideal recombination properties for the CBTSSe absorber layer.

4. Moving beyond CBTSSe

While CBTSSe provides an interesting paradigm for targeting PV performance using earth-abundant multinary chalcogenides, the broader I_2-II-IV-X_4 (with larger II atom) materials space is expected to offer further important opportunities. The crystal and band structures for 16 quaternary systems within the materials family, I_2-II-IV-X_4 (I = Cu, Ag; II = Sr, Ba; IV = Ge, Sn; *X* = S, Se), were investigated by Zhu *et al.*[102] using DFT calculations. The authors find that, depending on constituting elements, these compounds form in 5 different structure types (**Figure 11**) – i.e., orthorhombic $Ama2$ (e.g., $Cu_2BaSnSe_4$), trigonal $P3_1$ (e.g., Cu_2BaSnS_4), related trigonal $P3_2$ (e.g., Cu_2SrGeS_4), orthorhombic $I222$ (e.g., $Ag_2BaGeSe_4$), and tetragonal $I\bar{4}2m$ (e.g., Ag_2BaGeS_4). Among these 16 compounds, Ag-containing versions (i.e., forming in $I222$ and $I\bar{4}2m$ space groups) exhibit substantially indirect bandgaps ranging between 0.66 eV and 1.38 eV, with multivalley nature in the band structure, potentially useful for thermoelectric applications and perhaps less promising for PV. In contrast, Cu-containing compounds (i.e., forming in $Ama2$ and

$P3_1/P3_2$) show either direct or nearly direct (quasi-direct) bandgaps. Among Cu-containing compounds, $Cu_2BaGeSe_4$ (CBGSe) and Cu_2SrSnS_4 (CSTS) form in the $P3_1$ structure type (like CBTS) and offer calculated quasi-direct bandgaps of 1.60 eV and 1.73 eV, respectively—i.e., suitable values for multijunction PV (given that the DFT-derived bandgaps typically underestimate the experimental values). The authors also synthesized CBGSe powder and examined the optical bandgap with diffuse reflectance and PL measurements, yielding E_g = 1.91 eV—i.e., 0.31 eV larger than the DFT-predicted value.

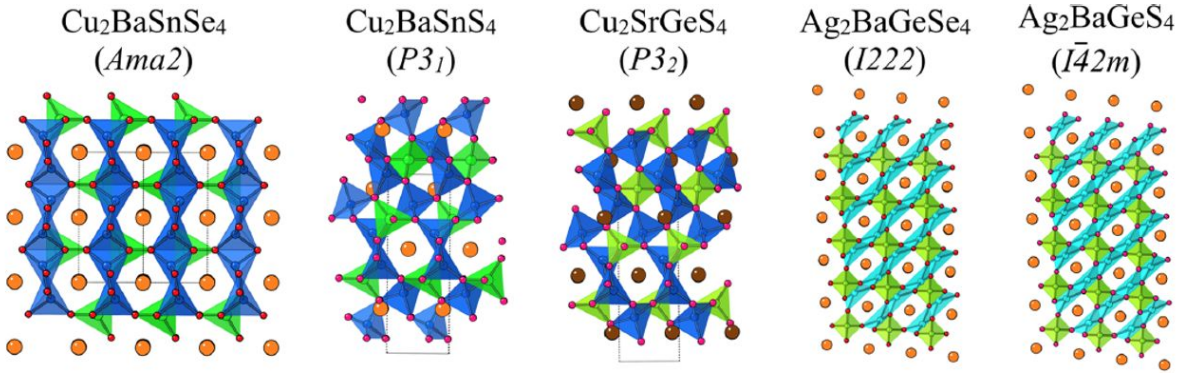

Figure 11 Crystal structures and associated space groups for five representative structure types encountered within the 16-compound group I_2–II–IV–VI_4 (I = Cu, Ag; II = Sr, Ba; IV = Ge, Sn; VI = S, Se). The I (Cu/Ag), II (Sr/Ba), IV (Ge/Sn), and VI (S/Se) atoms and their corresponding coordination polyhedra are shown in blue/light blue, brown/orange, light green/green, and light red/red, respectively. Reprinted with permission from ref.[102] Copyright 2017 American Chemical Society.

Kim *et al.*[134] reported the first films and PV devices based on CBGSe, which offers a similar bandgap and the same crystal structure type as for CBTS.[102,135] The authors examined overall optoelectronic properties for these films and compared with CBTS, prepared using a comparable vacuum-based film processing method. Hall effect measurements show that CBGSe has orders of magnitude higher hole carrier densities, while having more limited Hall mobilities ($p = 2.8\times10^{15}$ cm^{-3}; $\mu_H = 0.6$ $cm^2/V{\cdot}s$) relative to CBTS ($p = 5.3\times10^{12}$ cm^{-3}; $\mu_H = 3.5$ $cm^2/V{\cdot}s$). The authors also assessed recombination properties using optical pump terahertz probe spectroscopy (OPTP). Both CBGSe and CBTS yield comparable photoconductivity transient curves with two lifetime components (~10 ps and ~1-2 ns) (**Figure 12a**). While the faster photoconductivity decay may arise from a high surface recombination (as discussed earlier for CBTSSe), the longer component has been attributed to a bulk lifetime, suggesting that both materials have comparable limited minority carrier lifetimes. Intragrain sum mobilities determined from OPTP are 11 $cm^2/V{\cdot}s$ for CBGSe and 24 $cm^2/V{\cdot}s$ for CBTS. Overall, both lifetime and mobility values for CBGSe and CBTS are relatively modest compared to kesterite CZTS (~4 ns, and ~135 $cm^2/V{\cdot}s$), indicating that these materials (at least with the currently developed processing conditions and methods) may have relatively high densities of defects that limit both lifetime and mobility of charge carriers despite reduce band tailing.

Defect properties were further assessed using temperature-dependent PL (**Figure 12b-d**).[134] Both CBGSe and CBTS exhibit near band-edge emission at room temperature (given exciton

binding energies of ~20-25 meV). Upon cooling, CBGSe shows only free exciton (FX) emission, while the CBTS film exhibits both free and bound exciton (BX) features at the lowest temperature examined (21 K). Additionally, CBGSe offers a shallow-level defect emission peak at a relatively shallower energetic position than for CBTS (**Figure 12b**), possibly contributing to the higher hole carrier density for this system. However, CBGSe also exhibits a strong emission peak at an energetically deeper position, implying that CBGSe may have a higher density of deep-level defects that may act as recombination centers and limit bulk recombination properties. Beyond PL-based defect studies, the EA values measured from UPS/IPES are 3.7 eV for CBGSe and 3.3 eV for CBTS. Despite the larger value, CBGSe still has noticeably lower EA than CdS (**Figure 12e**), which may lead to substantial cliff-type CBO (as for CBTSSe) and implying that CBGSe solar cells should also require development of a suitable low EA buffer layer for optimizing band alignment. The first CBGSe solar cells based on conventional CBD-CdS buffer layers were also demonstrated, and exhibited a maximum of 1.5 % *PCE* (with V_{OC} = 623 mV), after a post-annealing treatment at 200°C, comparable to analogous CBTS solar cells (*PCE* = 1.6 %).[106]

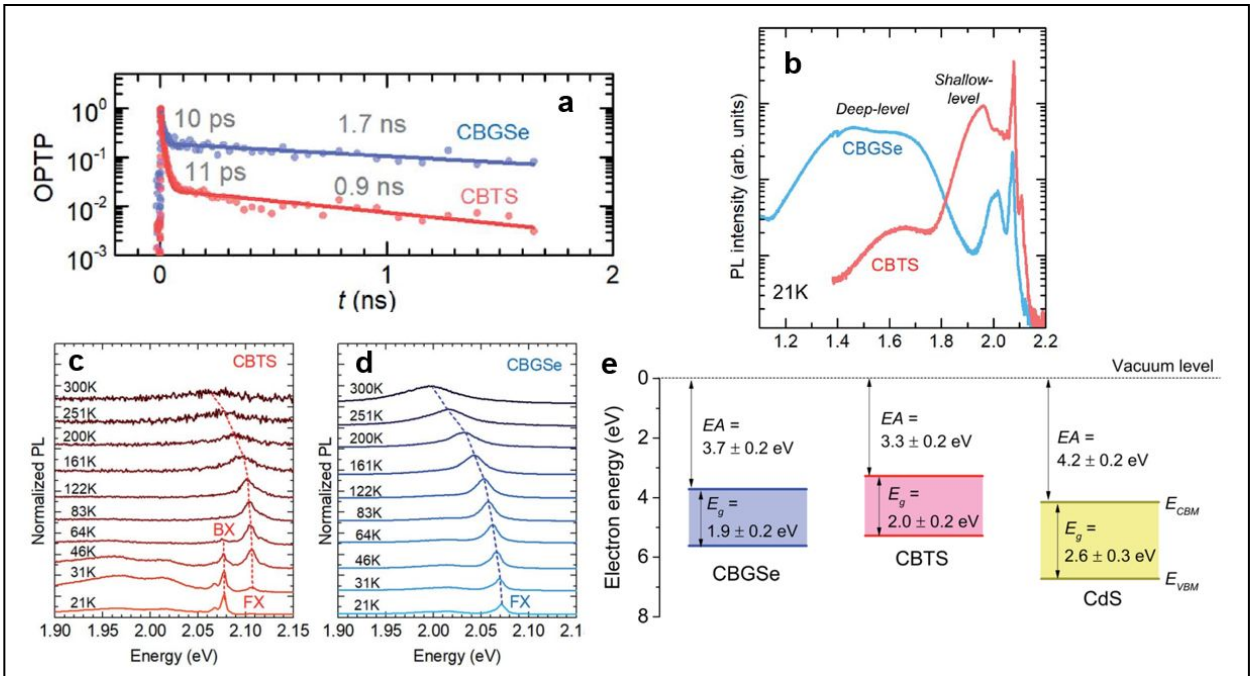

Figure 12 (a) Photoconductivity transient curves and (b) low temperature (21 K) PL spectra for CBTS and CBGSe showing both deep- and shallow-level defect emission. Temperature-dependent PL spectra for (c) CBGSe and (d) CBGTSe films. (e) E_{CBM} and E_{VBM} positions for CBGSe and CBTS (CdS is also shown for comparison). Panels (a-e) are reprinted from ref. [134], with permission from the Royal Society of Chemistry.

The bandgap for CBGSe is higher than the optimal range for single-junction solar cells under AM 1.5G illumination.[125] Partial substitution of Ge with Sn in CBGSe to form $Cu_2BaGe_{1-x}Sn_xSe_4$ (CBGTSe) has been suggested as an approach to tune the crystal lattice parameters and bandgap,[136] similar to partially substituting S with Se for CBTS (to form CBTSSe). According to this report, depending on the Sn/(Sn+Ge) elemental ratio (i.e., *x* value), CBGTSe crystallizes in either the trigonal ($P3_1$) or orthorhombic (*Ama2*) structure type; the bandgap can be reduced to 1.57 eV for

x = 0.7 while maintaining the trigonal crystal structure. CBGTSe films (x = 0.5 – 0.6) have been prepared by selenizing Cu–Ba–Ge–Sn precursor multilayers that were sequentially deposited using vacuum-based techniques, including both sputtering (for Cu, Ge and Sn) and evaporation (for Ba).[137] Vacuum-deposition of related Cu_2-*II*-*IV*-X_4 films (i.e., CBTS,[106,132,138] CBTSSe,[105,139,140] and CSTS[141]) to yield functioning solar cells has only been demonstrated using the co-sputtering approach. The challenges associated with high quality film growth from sequential deposition of elemental layers have been attributed in part to issues related to the alkaline earth element (e.g., Ba).[142] Kim and Mitzi's study[137] showed that such issues can be prevented using a high temperature vacuum pre-annealing step to partially homogenize the metallic precursor layer. The CBGTSe films exhibit a PL peak centered at 1.67 eV at room temperature, which is at a lower energy than for CBGSe (1.96 eV), reflecting an ~0.3 eV bandgap reduction via partial substitution of Ge with Sn. Additionally, the first prototype CBGTSe solar cells were recently demonstrated, yielding a maximum *PCE* of 3.1 %, after a post-annealing treatment at 200°C. However, as indicated by short minority carrier lifetime (**Figure 12a**) and low electron affinity (**Figure 12e**), both interface and bulk properties for the CBGSe and CBGTSe solar cells are likely culprits for the low performance, indicating the need for developing defect passivation strategies and low electron affinity buffer materials for further PV performance improvement.

Crovetto *et al*.[141] prepared Cu_2SrSnS_4 (CSTS) films using a vacuum-based technique, which involved co-sputtering of Cu, Sr and Sn targets under a mixture of Ar and O_2 to form Cu_2SrSnO_4 precursor films, followed by heating the films at 520°C under H_2S and Ar atmosphere to convert the layer into CSTS.[141] The bandgap for CSTS films derived from PL, optical absorption, and EQE (from solar cells) ranged over 1.93 eV – 1.98 eV (**Figure 13a**), approximately 0.20 eV – 0.25 eV higher than the DFT-computed value (consistent with the general trend comparing DFT with experimental values).[102] A solar cell with maximum efficiency of 0.59 % was demonstrated based on these CSTS films with CBD-CdS buffer layer (**Figure 13b, c**).[141] Later, Crovetto et al.[143] examined fundamental properties for CSTS and CBTS films. At low temperature (~80 K), both CSTS and CBTS films showed deep-level emission features at 1.4 eV – 1.6 eV (**Figure 13d**), which may reflect recombination centers that limit solar cell performance (comparable to similar features in **Figure 12b** for analogous comparison of CBGSe and CBTS[134]). The EA values, determined from XPS (ionization potential) and ellipsometry spectra (bandgap), are 3.66 eV for CSTS and 3.67 eV for CBTS (**Figure 13e**). These results, taken in aggregate with the EA measurements from other analogous studies, point to a general theme among the I_2-II-IV-X_4 (II = Sr, Ba) systems of low EA values for the prospective absorbers and a general need for developing suitable low-EA adjoining layers (buffer and window layers) that are chemically (reactivity) and energetically (band position) compatible with the absorbers.

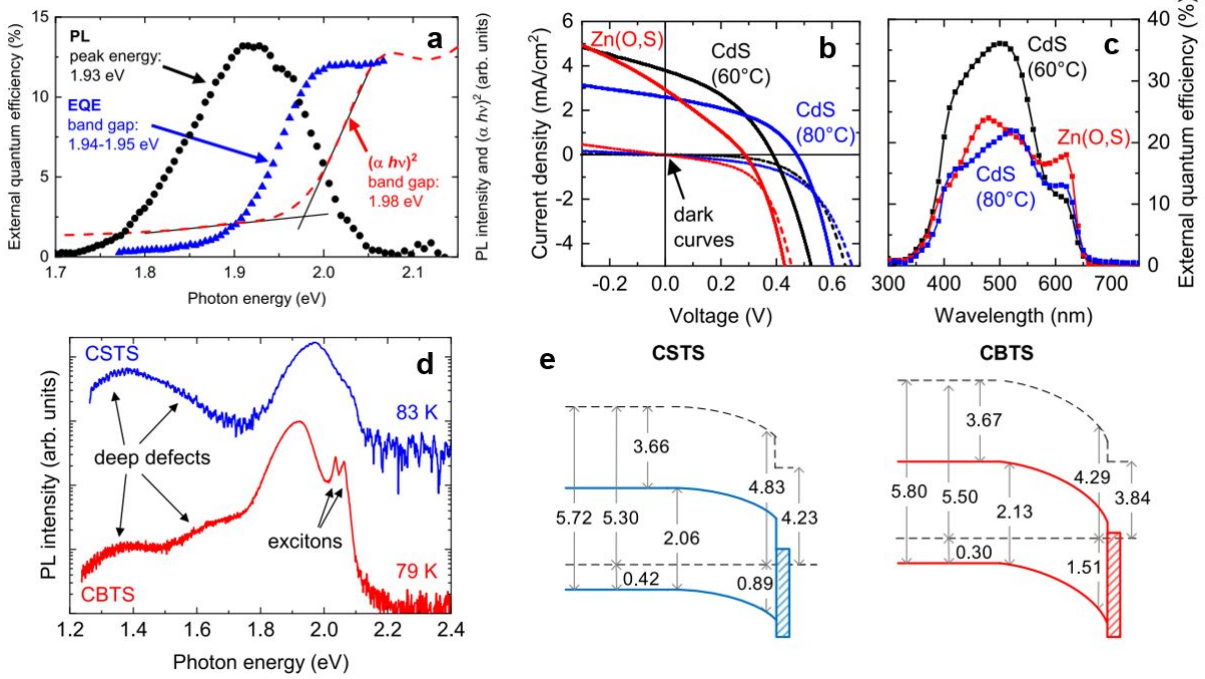

Figure 13 (a) Tauc plot and PL spectra of a CSTS film, and EQE onset of a CSTS solar cell. (b) Dark and light J-V and (c) EQE curves of three CSTS solar cells with differently processed buffer layers. The deposition temperatures for CBD-CdS are also indicated. Panels (a-c) are reprinted with permission from ref. [141]. Copyright 2019 American Chemical Society. **(d)** PL spectra of CSTS and CBTS films at temperatures of 83 K and 79 K, respectively. **(e)** Energy band diagrams of the bulk and surface of CSTS and CBTS determined from XPS and ellipsometry spectra. Panels (d) and (e) are reprinted with permission from ref. [143]. Copyright 2020 American Chemical Society.

Overall, despite the expected relatively high formation energies for group-2 (e.g., Sr, Ba) related anti-site defects, the limited measured bulk/surface properties (i.e., high density of deep-level defects) appear to be common issues for CBGSe, CSTS, and CBTS (and associated alloys). According to a study by Crovetto *et al.*[144] where chemical trends in the defect properties of Cu_2MSnS_4 (M = Zn, Cd, Sr, Ba) were examined by both experimental techniques and first-principles calculations, mitigation of band tailing from cation substitution does not imply suppression of non-radiative recombination. In fact, non-radiative recombination due to deep-level defects are more prominent in CBTS and CSTS than in CZTS. These results point to the need for an improved level of understanding and development of appropriate passivation strategies for deep-level defects in I_2-II-IV-X_4 (I = Cu, Ag; II = Sr, Ba; IV = Ge, Sn; X = S, Se) systems, to provide a pathway for improved PV performance. Further, recent efforts have been made to move beyond II = Sr, Ba systems to allow for a broader range of tunability in band positions and defect properties, and a structural tolerance factor approach has been developed to rationalize predicted structures based on constituent atoms (which in turn allows for predicting properties based on DFT approaches).[145] However, optoelectronic properties and prototype devices remain to be examined for these newer systems and this represents an important future direction.

5. Conclusions

Emerging thin-film elemental, binary and multinary chalcogenide absorbers present a compelling research direction for targeting the goal of low-cost and pervasive PV deployment. Among these, currently, only CZTS,[70] $Sb_2(S,Se)_3$,[34,35] and $Cu_{2-x}S$[14] have met or surpassed the *PCE* = 10% level. However, experiences with established high-performance systems such as CdTe and CIGS highlight the combined challenges of optimizing absorber chemistry/physics and overall device structure, and development times of decades are not unusual in the field. In this context, the above discussions point to numerous promising systems and pathways to pursue among chalcogenide absorbers and there arise some common themes for future needs: 1) Detailed fundamental studies and approaches to address band tailing, deep defect levels and recombination processes associated with absorbers and interfaces in device structures,[146] 2) understanding the sensitivity of the polycrystalline absorber films to growth conditions, preferred crystallographic orientation, detailed stoichiometry, and introduction of impurities (e.g., Na from the glass substrate), 3) addressing defect-related compensation mechanisms to allow for effective doping and Fermi level control within the emerging absorbers, 4) controlling interfacial chemistry issues at the absorber-charge transport layer (or buffer) interface, including reactivity, diffusion and band offsets, 5) demonstration of needed operational stability for the technologies (in contrast to the known stability issues for halide perovskite and $Cu_{2-x}S$ technologies[147,148]), and 6) consideration of how corresponding TFPV device materials and fabrication processes can be made to accommodate an environment-friendly and circular supply chain.[149,150]

Associated with the above discussion, there are also some key fundamental questions related to exploration for and development of emerging chalcogenide absorbers. For example, do we want to focus on 3D crystal structures (with associated 3D electronic dimensionality[151]) or can suitably oriented films of lower-dimensional structures provide a preferred pathway for reduced grain boundary and interfacial recombination (e.g., as argued for Sb_2Se_3)?[27] Is it preferrable to target simpler elemental/binary systems (e.g., Se, $Sb_2(S,Se)_3$, SnS, GeSe) that presumably offer less involved (and costly) processing or more complex multinary systems that provide a higher degree of prospective tunability with regards to band offsets, doping and related defect properties (e.g., CIGS, CZTS, CBTSSe, bournonite)? In the multinary systems, to what extent can coordination and atom size discrimination among the component elements be used to control adverse defect formation within the absorber and at interfaces (as argued for CBTSSe and related systems)?[77,106] Finally, given the extremely large phase space associated with the above optimizations, which includes a multitude of processing parameters, fundamental properties and device performance metrics, the question of whether and how combinatorial and machine learning (ML)/artificial intelligence(AI) approaches can practically provide a needed boost in development speed also represents an important consideration.[152-154] Notably, the above mentioned points are not unique to chalcogenide semiconductors and also are highly relevant for halide, pnictide and oxide absorber systems. Ultimately, addressing these questions/issues will hopefully enable TFPV to provide a viable pathway for more rapid PV deployment to help address the global climate crisis and need for clean energy sources.

Author contributions

All authors contributed to the writing of this review.

Conflicts of interest

There are no conflicts to declare.

Acknowledgements

This work was supported by the U. S. Department of Energy (DOE), Office of Science, Basic Energy Sciences (BES), under contract DE-SC0020061.

Notes and references

1. M. Victoria, N. Haegel, I. M. Peters, R. Sinton, A. Jäger-Waldau, C. del Cañizo, C. Breyer, M. Stocks, A. Blakers, I. Kaizuka, K. Komoto, A. Smets, *Joule*, 2021, 5, 1041-1056.

2. https://www.worldenergydata.org/world-electricity-generation (accessed 06/08/2022).

3. Photovoltaics Report, Fraunhofer Institute for Solar Energy Systems, ISE, 24 February 2022, https://www.ise.fraunhofer.de/content/dam/ise/de/documents/publications/studies/Photovoltaics-Report.pdf (accessed 6/8/2022).

4. A. Al-Ashouri, E. Köhnen, B. Li, A. Magomedov, H. Hempel, P. Caprioglio, J. A. Márquez, A. B. Morales Vilches, E. Kasparavicius, J. A. Smith, N. Phung, D. Menzel, M. Grischek, L. Kegelmann, D. Skroblin, C. Gollwitzer, T. Malinauskas, M. Jost, G. Matic, B. Rech, R. Schlatmann, M. Topic, L. Korte, A. Abate, B. Stannowski, D. Neher, M. Stolterfoht, T. Unold, V. Getautis, S. Albrecht, *Science*, 2020, 370, 1300-1309.

5. First Solar Annual Report 2021, https://s2.q4cdn.com/646275317/files/doc_financials/2021/ar/First-Solar-Annual-Report-2021-Web-version-(final-from-Merrill).pdf (accessed 06/08/2022).

6. D. C. Jordan, S. R. Kurtz, K. VanSant, J. Newmiller, *Prog. Photovolt. Res. Appl.*, 2016, 24, 978-989.

7. M. Powalla, S. Paetel, E. Ahlswede, R. Wuerz, C. D. Wessendorf, T. M. Friedlmeier, *Appl. Phys. Rev.*, 2018, 5, 041602.

8. J. W. Choi, B. Shin, P. Gorai, R. L. Z. Hoye, R. Palgrave, *ACS Energy Lett*., 2022, 7, 1553-1557.

9. S. Hadke, M. Huang, C. Chen, Y. F. Tay, S. Chen, J. Tang, L. Wong, *Chem. Rev.*, 2022, 122, 10170-10265.

10. P. K. Nayak, S. Mahesh, H. J. Snaith, D. Cahen, *Nat. Rev. Mater.*, 2019, 4, 269-285.

11. F. Liu, Q. Zeng, J. Li, X. Hao, A. Ho-Baillie, J. Tang, M. A. Green, *Mater. Today,* 2020, 41, 120-142.

12. W. Yang, X. Zhang, S. D. Tilley, *Chem. Mater.*, 2021, 33, 3467-3489.

13. L. C. Burton, *Solar Cells*, 1979/1980, 1, 159-174.

14. R. B. Hall, R. W. Birkmire, J. E. Phillips, J. D. Meakin, *Appl. Phys. Lett.*, 1981, 38, 925-926.

15. T. K. S. Wong, S. Zhuk, S. Masudy-Panah, G. K. Dalapati, *Materials*, 2016, 9, 271.

16. C. Steinhagen, T. B. Harvey, C. J. Stolle, J. Harris, B. A. Korgel, *J. Phys. Chem. Lett.*, 2012, 3, 2352-2356.

17. M. Rahman, G. Boschloo, A. Hagfeldt, T. Edvinsson, *Adv. Mater.*, 2020, 32, 1905653.

18. S. Aina, B. Villacampa, M. Bernechea, *Mater. Adv.,* 2021, 2, 4140-4151.

19. O. Stroyuk, A. Raevskaya, N. Gaponik, *Chem. Soc. Rev.* 2018, 47, 5354-5422.

20. J. Tang, K. W. Kemp, S. Hoogland, K. S. Jeong, H. Liu, L. Levina, M. Furukawa, X. Wang, R. Debnath, D. Cha, K. W. Chou, A. Fischer, A. Amassian, J. B. Asbury, E. H. Sargent, *Nature Mater.*, 2011, 10, 765-771.

21. L. Yu, R. S. Kokenyesi, D. A. Keszler, A. Zunger, *Adv. Energy Mater.*, 2012, 3, 43-48.

22. A. Zakutayev, C. M. Caskey, A. N. Fioretti, D. S. Ginley, J. Vidal, V. Stevanovic, E. Tea, S. Lany, *J. Phys. Chem. Lett.*, 2014, 5, 1117-1125.

23. K. Choudhary, M. Bercx, J. Jiang, R. Pachter, D. Lamoen, *Chem. Mater.*, 2019, 31, 5900-5908.

24. R. Kondrotas, C. Chen, J. Tang, *Joule*, 2018, 2, 857-878.

25. C. Chen, K. Li, J. Tang, *Solar RRL*, 2022, https://doi.org/10.1002/solr.202200094 (published on-line as ASAP article).

26. U. A. Shah, S. Chen, G. M. G. Khalaf, Z. Jin, H. Song, *Adv. Funct. Mater.*, 2021, 31, 2100265.

27. Y. Zhou, L. Wang, S. Chen, S. Qin, X. Liu, J. Chen, D.-J. Xue, M. Luo, Y. Cao, Y. Cheng, E. H. Sargent, J. Tang, *Nature Photonics*, 2015, 9, 409-415.

28. Y. C. Choi, D. U. Lee, J. H. Noh, E. K. Kim, S. I. Seok, *Adv. Funct. Mater*., 2014, 24, 3587-3592.

29. J. Han, X. Pu, H. Zhou, Q. Cao, S. Wang, Z. He, B. Gao, T. Li, J. Zhao, X. Li, *ACS Appl. Mater. Interfaces*, 2020, 12, 44297-44306.

30. T. Fujita, K. Kurita, K. Takiyama, T. Oda, *J. Phys. Soc. Jpn.*, 1987, 56, 3734-3739.

31. P. Myagmarsereejid, M. Ingram, M. Batmunkh, Y. L. Zhong, *Small*, 2021, 17, 2100241.

32. W. Lian, C. Jiang, Y. Yin, R. Tang, G. Li, L. Zhang, B. Che, T. Chen, *Nature Commun*., 2021, 12, 3260.

33. Z. Li, X. Liang, G. Li, H. Liu, H. Zhang, J. Guo, J. Chen, K. Shen, X. San, W. Yu, R. E. I. Schropp, Y. Mai, *Nature Commun.*, 2019, 10, 125.

34. R. Tang, X. Wang, W. Lian, J. Huang, Q. Wei, M. Huang, Y. Yin, C. Jiang, S. Yang, G. Xing, S. Chen, C. Zhu, X. Hao, M. A. Green, T. Chen, *Nature Energy*, 2020, 5, 587-595.

35. Y. Zhao, S. Wang, C. Jiang, C. Li, P. Xiao, R. Tang, J. Gong, G. Chen, T. Chen, J. Li, X. Xiao, *Adv. Energy Mater*., 2022, 12, 2103015.

36. S. Barthwal, R. Kumar, S. Pathak, *ACS Appl. Energy Mater.*, 2022, https://doi.org/10.1021/acsaem.2c00420 (published on-line as ASAP article).

37. K. Zeng, D. J. Xue, J. Tang, *Semicond. Sci. Technol.*, 2016, 31, 063001.

38. Z. Yang et. al., *Nature Commun.*, 2019, 10, 4540.

39. J. R. Brent, D. J. Lewis, T. Lorenz, E. A. Lewis, N. Savjani, S. J. Haigh, G. Seifert, B. Derby, P. O'Brian, *J. Am. Chem. Soc.*, 2015, 137, 12689-12696.

40. T. Jiang, G. A. Ozin, *J. Mater. Chem.*, 1998, 8, 1099-1108.

41. P. Sinsermsuksakul, L. Sun, S. W. Lee, H. H. Park, S. B. Kim, C. Yang, R. G. Gordon, *Adv. Energy Mater.*, 2014, 4, 1400496.

42. R. E. Banai, M. W. Horn, J. R. S. Brownson, *Sol. Energy Mater. Sol. Cells*, 2016, 150, 112–129.

43. P. Sinsermsuksakul, K. Hartman, S. B. Kim, J. Heo, L. Sun, H. H. Park, R. Chakraborty, T. Buonassisi, R. G. Gordon, *Appl. Phys. Lett.*, 2013, 102, 053901.

44. T. Ikuno, R. Suzuki, K. Kitazumi, N. Takahashi, N. Kato, K. Higuchi, *Appl. Phys. Lett.*, 2013, 102, 193901.

45. H.-S. Yun, B.-W. Park, Y. C. Choi, J. Im, T. J. Shin, S. I. Seok, *Adv. Energy Mater.*, 2019, 9, 1901343.

46. J. Y. Cho, S. Y. Kim, R. Nandi, J. Jang, H.-S. Yun, E. Enkhbayar, J. H. Kim, D.-K. Lee, C.-H. Chung, J. H. Kim, J. Heo, *J. Mater. Chem. A*, 2020, 8, 20658-20665.

47. S. Kawanishi, I. Suzuki, S. R. Bauers, A. Zakutayev, H. Shibata, H. Yanagi, T. Omata, *Solar RRL*, 2021, 5, 2000708.

48. T. R. Rana, S. Kim, J. Kim, *Current Appl. Phys*., 2018, 18, 663-666.

49. S.-C. Liu, Y. Yang, Z. Li, D. J. Xue, J.-S. Hu, *Mater. Chem. Front.*, 2020, 4, 775-787.

50. S.-C. Liu, C.-M. Dai, Y. Min, Y. Hou, A. H. Proppe, Y. Zhou, C. Chen, S. Chen, J. Tang, D.-J. Xue, E. H. Sargent, J.-S. Hu, *Nat. Commun*. 2021, 12, 670.

51. D.-J. Xue, S.-C. Liu, C.-M. Dai, S. Chen, C. He, L. Zhao, J.-S. Hu, L.-J. Wan, *J. Am. Chem. Soc.*, 2017, 139, 958-965.

52. J.-M. Wu, Y.-P. Lv, H. Wu, H.-S. Zhang, F. Wang, J. Zhang, J.-Z. Wang, X.-H. Xu, *Rare Metals*, 2022, ASAP article, DOI: 10.1007/s12598-022-02005-1.

53. R. Nandi, P. S. Pawar, K. E. Neerugatti, J. Y. Cho, S. Kim, S. H. Cho, Y. S. Lee, J. Heo, *Solar RRL*, 2021, 6, 2100676.

54. T. H. Youngman, R. Nielsen, A. Crovetto, B. Seger, O. Hansen, I. Chorkendorff, P. C. K. Vesborg, *Solar RRL*, 2021, 5, 2100111.

55. J. J. Dowd, *Proc. Phys. Soc. B*, 1951, 64, 783-789.

56. A. Kunioka, T. Nakada, *Jpn. J. Appl. Phys.*, 1982, 21, 73-75.

57. T. Nakada, A. Kunioka, *Jpn. J. Appl. Phys.*, 1985, 24, L536-L538.

58. T. K. Todorov, S. Singh, D. M. Bishop, O. Gunawan, Y. S. Lee, T. S. Gershon, K. W. Brew, P. D. Antunez, R. Haight, *Nat. Commun.*, 2017, 8, 682.

59. R. Nielsen, T. H. Youngman, A. Crovetto, O. Nansen, I. Chorkendorff, P. C. K. Vesborg, *ACS Appl. Energy Mater.*, 2021, 4, 10697-10702.

60. W. Liu, A. A. Said, W. J. Fan, Q. Zhang, *ACS Appl. Energy Mater.*, 2020, 3, 7345-7352.

61. I. Hadar, T.-B. Song, W. Ke, M. Kanatzidis, *Adv. Energy Mater.*, 2019, 9, 1802766.

62. P. Cherin, P. Unger, *Inorg. Chem.*, 1967, 6, 1589-1591.

63. I. Hadar, X. Hu, Z.-Z. Luo, V. P. Dravid, M. G. Kanatzidis, *ACS Energy Lett.*, 2019, 4, 2137.

64. S. D. Deshmukh, C. K. Miskin, A. A. Pradhan, K. Kisslinger, R. Agrawal, *ACS Appl. Energy Mater.*, 2022, 5, 3275-3281.

65. F. Larsson, N. S. Nilsson, J. Keller, C. Frisk, V. Kosyak, M. Edoff, T. Törndahl, *Prog. Photovolt. Res. Appl.*, 2017, 25, 755-763.

66. M. Nakamura, N. Yoneyama, K. Horiguchi, Y. Iwata, K. Yamaguchi, H. Sugimoto, T. Kato, *2014 IEEE 40th Photovoltaic Specialist Conference (PVSC)*, 2014, pp. 0107-0110.

67. M. He, C. Yan, J. Li, M. P. Suryawanshi, J. Kim, M. A. Green, X. Hao, *Adv. Science*, 2021, 8, 2004313.

68. D. B. Mitzi, O. Gunawan, T. K. Todorov, K. Wang, S. Guha, *Sol. Energy Mater. Sol. Cells*, 2011, 95, 1421-1436.

69. K. Ito, T. Nakazawa, *Jpn. J. Appl. Phys.*, 1988, 27, 2094-2097.

70. W. Wang, M. T. Winkler, O. Gunawan, T. Gokmen, T. K. Todorov, Y. Zhu, D. B. Mitzi, *Adv. Energy Mater.*, 2014, 4, 1301465.

71. M. A. Green, E. D. Dunlop, J. Hohl-Ebinger, M. Yoshita, N. Kopidakis, X. Hao, *Prog. Photovolt. Res. Appl.*, 2022, 30, 687-701.

72. S. Bourdais, C. Choné, B. Delatouche, A. Jacob, G. Larramona, C. Moisan, A. Lafond, F. Donatini, G. Rey, S. Siebentritt, *Adv. Energy Mater.*, 2016, 6, 1502276.

73. D. B. Mitzi, O. Gunawan, T. K. Todorov, D. A. R. Barkhouse, *Philos. Trans. R. Soc. A*, 2013, 371, 20110432.

74. S. Chen, X. Gong, A. Walsh, S.-H. Wei, *Appl. Phys. Lett.*, 2009, 94, 041903.

75. S. Chen, A. Walsh, X. G. Gong, S. H. Wei, *Adv. Mater.*, 2013, 25, 1522-1539.

76. S. Chen, X. Gong, A. Walsh, S.-H. Wei, *Appl. Phys. Lett.*, 2010, 96, 021902.

77. D. Shin, B. Saparov, D. B. Mitzi, *Adv. Energy Mater.*, 2017, 7, 1602366.

78. T. Gokmen, O. Gunawan, T. K. Todorov, D. B. Mitzi, *Appl. Phys. Lett.*, 2013, 103, 103506.

79. J. E. Moore, C. J. Hages, R. Agrawal, M. S. Lundstrom, J. L. Gray, *Appl. Phys. Lett.*, 2016, 109, 021102.

80. S. Schorr, *Sol. Energy Mater. Sol. Cells*, 2011, 95, 1482-1488.

81. S. Chen, L.-W. Wang, A. Walsh, X. Gong, S.-H. Wei, *Appl. Phys. Lett.*, 2012, 101, 223901.

82. K. Biswas, S. Lany, A. Zunger, *Appl. Phys. Lett.*, 2010, 96, 201902.

83. G. Rey, A. Redinger, J. Sendler, T. P. Weiss, M. Thevenin, M. Guennou, B. El Adib, S. Siebentritt, *Appl. Phys. Lett.*, 2014, 105, 112106.

84. T. Gershon, Y. S. Lee, P. Antunez, R. Mankad, S. Singh, D. Bishop, O. Gunawan, M. Hopstaken, R. Haight, *Adv. Energy Mater.*, 2016, 6, 1502468.

85. J. J. Scragg, L. Choubrac, A. Lafond, T. Ericson, C. Platzer-Björkman, *Appl. Phys. Lett.*, 2014, 104, 041911.

86. C. Krämmer, C. Huber, C. Zimmermann, M. Lang, T. Schnabel, T. Abzieher, E. Ahlswede, H. Kalt, M. Hetterich, *Appl. Phys. Lett.*, 2014, 105, 262104.

87. J. J. Scragg, J. K. Larsen, M. Kumar, C. Persson, J. Sendler, S. Siebentritt, C. Platzer Björkman, *Phys. Stat. Sol.(b)*, 2016, 253, 247-254.

88. T. Gershon, D. Bishop, B. McCandless, W. Wang, R. Haight, *Proc. SPIE 9552, Carbon Nanotubes, Graphene, and Emerging 2D Materials for Electronic and Photonic Devices VIII*, 2015, pp. 955209.

89. G. H. Vineyard, *Phys. Rev.*, 1956, 102, 981.

90. T. Gershon, K. Sardashti, O. Gunawan, R. Mankad, S. Singh, Y. S. Lee, J. A. Ott, A. Kummel, R. Haight, *Adv. Energy Mater.*, 2016, 6, 1601182.

91. Z. Su, J. M. R. Tan, X. Li, X. Zeng, S. K. Batabyal, L. H. Wong, *Adv. Energy Mater.*, 2015, 5, 1500682.

92. C. Yan, K. Sun, J. Huang, S. Johnston, F. Liu, B. P. Veettil, K. Sun, A. Pu, F. Zhou, J. A. Stride, *ACS Energy Lett.*, 2017, 2, 930-936.

93. R. R. Prabhakar, S. Zhenghua, Z. Xin, T. Baikie, L. S. Woei, S. Shukla, S. K. Batabyal, O. Gunawan, L. H. Wong, *Sol. Energy Mater. Sol. Cells*, 2016, 157, 867-873.

94. X. Meng, H. Deng, J. He, L. Sun, P. Yang, J. Chu, *Mater. Lett*., 2015, 151, 61-63.

95. B. Murali, M. Madhuri, S. Krupanidhi, *Cryst. Growth Des*., 2014, 14, 3685-3691.

96. J. Schneider, H. Müller, K. Maier, W. Wilkening, F. Fuchs, A. Dörnen, S. Leibenzeder, R. Stein, *Appl. Phys. Lett*., 1990, 56, 1184-1186.

97. J. Baur, K. Maier, M. Kunzer, U. Kaufmann, J. Schneider, H. Amano, I. Akasaki, T. Detchprohm, K. Hiramatsu, *Appl. Phys. Lett*., 1994, 64, 857-859.

98. R. Korotkov, J. Gregie, B. Wessels, *MRS Online Proceedings Library (OPL)*, 2000, 639.

99. J. Fu, D. Kou, W. Zhou, Z. Zhou, S. Yuan, Y. Qi, S. Wu, *J. Mater. Chem. A*, 2020, 8, 22292-22301.

100. S. Kim, K. M. Kim, H. Tampo, H. Shibata, S. Niki, *Appl. Phys. Expr.*, 2016, 9, 102301.

101. R. D. Shannon, *Acta Crystallogr. A*, 1976, 32, 751-767.

102. T. Zhu, W. P. Huhn, G. C. Wessler, D. Shin, B. Saparov, D. B. Mitzi, V. Blum, *Chem. Mater.*, 2017, 29, 7868-7879.

103. F. Hong, W. Lin, W. Meng, Y. Yan, *PCCP*, 2016, 18, 4828-4834.

104. B. Teymur, Y. Zhou, E. Ngaboyamahina, J. T. Glass, D. B. Mitzi, *Chem. Mater.*, 2018, 30, 6116-6123.

105. D. Shin, T. Zhu, X. Huang, O. Gunawan, V. Blum, D. B. Mitzi, *Adv. Mater.*, 2017, 29, 1606945.

106. D. Shin, B. Saparov, T. Zhu, W. P. Huhn, V. Blum, D. B. Mitzi, *Chem. Mater.*, 2016, 28, 4771-4780.

107. D. Shin, E. Ngaboyamahina, Y. Zhou, J. T. Glass, D. B. Mitzi, *J. Phys. Chem. Lett*., 2016, 7, 4554-4561.

108. S. K. Wallace, K. L. Svane, W. P. Huhn, T. Zhu, D. B. Mitzi, V. Blum, A. Walsh, *Sustain. Energy Fuels*, 2017, 1, 1339-1350.

109. S. K. Wallace, K. T. Butler, Y. Hinuma, A. Walsh, *J. Appl. Phys.*, 2019, 125, 055703.

110. Y. Liu, B. Yang, M. Zhang, B. Xia, C. Chen, X. Liu, J. Zhong, Z. Xiao, J. Tang, *Nano Energy*, 2020, 71, 104574.

111. M. Zhang, Y. Liu, B. Yang, X. Lin, Y. Lu, J. Zheng, C. Chen, J. Tang, *ACS Appl. Mater*. Interfaces, 2021, 13, 13273-13280.

112. A. Kojima, K. Teshima, Y. Shirai, T. Miyasaka, *J. Am. Chem. Soc.*, 2009, 131, 6050-6051.

113. A. K. Jena, A. Kulkami, T. Miyasaka, *Chem. Rev.*, 2019, 119, 3036-3103.

114. P. Basumatary, P. Agarwal, *Mater. Res. Bull.*, 2022, 149, 111700.

115. T. Leijtens, K. A. Bush, R. Prasanna, M. D. McGehee, *Nature Energy*, 2018, 3, 828-838.

116. S. Rühle, *Solar Energy*, 2016, 130, 139-147.

117. W.-J. Yin, T. Shi, Y. Yan, *Adv. Mater.*, 2014, 26, 4653–4658.

118. W. A. Dunlap-Shohl, Y. Zhou, N. P. Padture, D. B. Mitzi, *Chem. Rev.*, 2019, 119, 3193−3295.

119. D. Tiwari, O. S. Hutter, G. Longo, *J. Phys. Energy*, 2021, 3, 034010.

120. K. V. Sophia, C. Comparotto, J. A. Márquez, J. J. S. Scragg, *Adv. Opt. Mater*., 2022, 10, 2101704.

121. E. Z. Stutz, M. Zamani, D. A. Damry, L. Buswell, R. Paul, S. E. Steinvall, J.-B. Leran, J. L. Boland, M. Dimitrievska, A. F. i Morral, *Mater. Adv.*, 2022, 3, 1295-1303.

122. T. Kuwano, R. Katsube, K. Kazumi, Y. Nose, *Sol. Energy Mater. Solar Cells*, 2021, 221, 110891.

123. K. Javaid, W. Wu, J. Wang, J. Fang, H. Zhang, J. Gao, F. Zhuge, L. Liang, H. Cao, *ACS Photonics*, 2018, 5, 2094−2099.

124. M. Bhushan, A. Catalano, *Appl. Phys. Lett.*, 1981, 38, 39-41.

125. W. Shockley, H. J. Queisser, *J. Appl. Phys.*, 1961, 32, 510-519.

126. K. Sardashti, R. Haight, T. Gokmen, W. Wang, L. Y. Chang, D. B. Mitzi, A. C. Kummel, *Adv. Energy Mater.*, 2015, 5, 1402180.

127. B. Teymur, S. Levcenco, H. Hempel, E. Bergmann, J. A. Márquez, L. Choubrac, I. G. Hill, T. Unold, D. B. Mitzi, *Nano Energy*, 2020, 80, 105556.

128. H. Hempel, C. J. Hages, R. Eichberger, I. Repins, T. Unold, *Scient. Reports*, 2018, 8, 1-9.

129. S. Levcenko, B. Teymur, D. Mitzi, T. Unold, *APL Mater.*, 2021, 9, 111108.

130. T. Minemoto, T. Matsui, H. Takakura, Y. Hamakawa, T. Negami, Y. Hashimoto, T. Uenoyama, M. Kitagawa, *Sol. Energy Mater. Sol. Cells*, 2001, 67, 83-88.

131. E. Ghorbani, *J. Phys.: Energy*, 2020, 2, 025002.

132. J. Ge, P. Koirala, C. R. Grice, P. J. Roland, Y. Yu, X. Tan, R. J. Ellingson, R. W. Collins, Y. Yan, *Adv. Energy Mater.*, 2017, 7, 1601803.

133. B. Teymur, Y. Kim, J. Huang, K. Sun, X. Hao, D. B. Mitzi, *Submitted*, 2022.

134. Y. Kim, H. Hempel, S. Levcenko, J. Euvrard, E. Bergmann, G. Oki, T. Unold, I. G. Hill, D. B. Mitzi, *J. Mater. Chem. A*, 2021, 9, 23619-23630.

135. M. Tampier, D. Johrendt, *Z. Anorg. Allg. Chem.*, 2001, 627, 312-320.

136. G. C. Wessler, T. Zhu, J.-P. Sun, A. Harrell, W. P. Huhn, V. Blum, D. B. Mitzi, *Chem. Mater.*, 2018, 30, 6566-6574.

137. Y. Kim, D. B. Mitzi, *ACS Appl. Energy Mater*., 2021, 4, 11528-11536.

138. H. Guo, C. Ma, Z. Chen, X. Jia, Q. Cang, N. Yuan, J. Ding, *Solar Energy*, 2019, 181, 301-307.

139. D. Shin, E. Ngaboyamahina, Y. Zhou, J. T. Glass, D. B. Mitzi, *J. Phys. Chem. Lett.*, 2016, 7, 4554-4561.

140. J. Ge, Y. Yu, Y. Yan, *ACS Energy Lett.*, 2016, 1, 583-588.

141. A. Crovetto, R. Nielsen, E. Stamate, O. Hansen, B. Seger, I. Chorkendorff, P. C. Vesborg, *ACS Appl. Energy Mater*., 2019, 2, 7340-7344.

142. J.-P. Sun, J. A. Márquez, H. Stange, R. Mainz, D. B. Mitzi, *Phys. Rev. Mater.*, 2019, 3, 055402.

143. A. Crovetto, Z. Xing, M. Fischer, R. Nielsen, C. N. Savory, T. Rindzevicius, N. Stenger, D. O. Scanlon, I. Chorkendorff, P. C. Vesborg, *ACS Appl. Mater. & Int.*, 2020, 12, 50446-50454.

144. A. Crovetto, S. Kim, M. Fischer, N. Stenger, A. Walsh, I. Chorkendorff, P. C. Vesborg, *Energy & Environ. Sci.*, 2020, 13, 3489-3503.

145. J.-P. Sun, G. C. McKeown Wessler, T. Wang, T. Zhu, V. Blum, D. B. Mitzi, *Chem. Mater*., 2020, 32, 1636.

146. J. S. Park, S. Kim, Z. Xie, A. Walsh, *Nat. Rev. Mater.*, 2018, 3, 194-210.

147. C. C. Boyd, R. Cheacharoen, T. Leijtens, M. D. McGehee, *Chem. Rev.*, 2019, 119, 3418-3451.

148. K. Moitra, S. Deb, *Solar Cells*, 1983, 9, 215-228.

149. J. A. Tsanakas, A. van der Heide, T. Radavičius, J. Denafas, E. Lemaire, K. Wang, J. Poortmans, E. Voroshazi, *Prog. Photovolt. Res. Appl.*, 2020, 28, 454-464.

150. D. Sica, O. Malandrino, S. Supino, M. Testa, M. C. Lucchetti, *Renew. Sust. Energy Rev.*, 2018, 82, 2934-2945.

151. Z. Xiao, W. Meng, J. Wang, D. B. Mitzi, Y. Yan, *Mater. Horiz.*, 2017, 4, 206-216.

152. K. Choudhary, M. Bercx, J. Jiang, R. Pachter, D. Lamoen, *Chem. Mater.*, 2019, 31, 5900-5908.

153. Z. Wang, J. Cai, Q. Wang, S. Wu, J. Li, *npj Comput. Mater.*, 2021, 7, 128.

154. A. Mannodi-Kanakkithodi, X. Xiang, L. Jacoby, R. Biegaj, S. T. Dunham, D. R.Gamelin, M. K. Y. Chan, *Patterns*, 2022, 3, 100450.